J. Fluid Mech. (2008), *vol.* 616, *pp.* 1–30.
doi:10.1017/S0022112008004060 Printed in the United Kingdom

Direct numerical simulation of wind-wave generation processes

MEI-YING LIN[1,3], CHIN-HOH MOENG[2]†, WU-TING TSAI[1,4], PETER P. SULLIVAN[2] AND STEPHEN E. BELCHER[5]

[1]Department of Civil Engineering, National Chiao Tung University, Hsinchu 30050, Taiwan

[2]National Center for Atmospheric Research, Boulder, Colorado 80307, USA

[3]Taiwan Typhoon and Flood Research Institute, Taichung 40763, Taiwan

[4]Institute of Hydrological Sciences, National Central University, Taoyuan 32001, Taiwan

[5]Department of Meteorology, University of Reading, Earley Gate, PO Box 243, Reading RG6 6BB, UK

(Received 6 June 2007 and in revised form 20 August 2008)

An air–water coupled model is developed to investigate wind-wave generation processes at low wind speed where the surface wind stress is about 0.089 dyn cm^{-2} and the associated surface friction velocities of the air and the water are $u_a^* \sim 8.6\,\mathrm{cm\,s^{-1}}$ and $u_w^* \sim 0.3\,\mathrm{cm\,s^{-1}}$, respectively. The air–water coupled model satisfies continuity of velocity and stress at the interface simultaneously, and hence can capture the interaction between air and water motions. Our simulations show that the wavelength of the fastest growing waves agrees with laboratory measurements ($\lambda \sim 8$–$12\,\mathrm{cm}$) and the wave growth consists of linear and exponential growth stages as suggested by theoretical and experimental studies. Constrained by the linearization of the interfacial boundary conditions, we perform simulations only for a short time period, about 70 s; the maximum wave slope of our simulated waves is $ak \sim 0.01$ and the associated wave age is $c/u_a^* \sim 5$, which is a slow-moving wave. The effects of waves on turbulence statistics above and below the interface are examined. Sensitivity tests are carried out to investigate the effects of turbulence in the water, surface tension, and the numerical depth of the air domain. The growth rates of the simulated waves are compared to a previous theory for linear growth and to experimental data and previous simulations that used a prescribed wavy surface for exponential growth. In the exponential growth stage, some of the simulated wave growth rates are comparable to previous studies, but some are about 2–3 times larger than previous studies. In the linear growth stage, the simulated wave growth rates for these four simulation runs are about 1–2 times larger than previously predicted. In qualitative agreement with previous theories for slow-moving waves, the mechanisms for the energy transfer from wind to waves in our simulations are mainly from turbulence-induced pressure fluctuations in the linear growth stage and due to the in-phase relationship between wave slope and wave-induced pressure fluctuations in the exponential growth stage.

1. Introduction

As wind flows over a water surface, air and water motions interact and induce many phenomena at the interface. Wind-generated waves are the most visible signature of

† Email address for correspondence: moeng@ucar.edu

this interaction and have a major influence on the momentum and energy transfer across the interface. These wind-generated waves, observed by microwave-radar backscatter, have wavelengths of the order of 4–40 cm (Massel 1996). Because these small-scale waves impact remote sensing of the sea surface, the generation and growth of wind-generated waves have been subjects of much research. However, the mechanisms that generate these surface waves are still an open issue owing to (i) difficulties in obtaining a dataset from laboratory and field measurements that records the time evolution of motions in both atmosphere and ocean domains; (ii) mathematical difficulties in dealing with highly turbulent flows over complex moving surfaces; and (iii) lack of a suitable coupled model to simulate turbulent flows in both atmosphere and ocean simultaneously. With increases in computer power, it is now possible to simulate wave and turbulence phenomenon by direct numerical simulation (DNS). DNS numerically solves the Navier–Stokes equation subject to boundary conditions, and hence such simulated flow fields contain no uncertainties other than numerical errors. In this study, we develop an air–water coupled DNS model and use it to study wind-wave generation and growth processes.

Theoretical studies (Jeffreys 1925; Miles 1957; Phillips 1957, 1977; Phillips & Katz 1961; Townsend 1972, 1980; Jacobs 1987; Kahma & Donelan 1988; van Duin & Janssen 1992; Belcher & Hunt 1993, among many others) have proposed different mechanisms as to how surface waves are generated from calm water and quantify the consequential growth rate of surface waves. These studies suggest that there are linear and exponential growth regimes for surface waves. Most of the previous numerical studies (Davis 1970; Gent & Taylor 1976; Al-Zanaidi & Hui 1984; De Angelis, Lombardi & Banerjee 1997; Henn & Sykes 1999; Sullivan, McWilliams & Moeng 2000; Tsai, Chen & Moeng 2005) examine either the wave effect on air motions or the wind stress effect on water motions by simulating only air or water flows (i.e. one-phase flow). Only a few numerical studies are conducted for two-phase flows (Lombardi, De Angelis & Banerjee 1996; De Angelis 1998; Fulgosi *et al.* 2003), but none of them investigate the wind-wave generation processes. The present study, therefore, is aimed at unravelling wind-wave generation processes by conducting direct numerical simulations that couple turbulent air and water flows.

The organization of this paper is as follows. The numerical aspects of the present simulation, including the model formulation, numerical method and simulation implementation are described in § 2. The simulated flow structures of surface waves and elongated streaks generated by wind are shown in § 3. The wave effect on the statistics of mean velocity and turbulent intensity is reported in § 4. The characteristics of the generated surface waves are examined in § 5. Two wave growth types are defined in § 6. Comparison with theoretical wind-wave generation mechanisms is given in § 7. The effects of turbulence in the water, surface tension, and the numerical domain in the air side on wave growth are examined in § 8. Finally, the main conclusions of this paper are reported in § 9.

2. The coupled model

2.1. *Flow configuration*

We consider two turbulent flows (air and water) interacting across a deformable interface under a wind-driven system. Each domain of the two immiscible fluids is a rectangular box with a depth h and horizontal length $(L_x, L_y) = 6h$ (figure 1). We adopt a Cartesian coordinate where the air region occupies the $z \geqslant 0$ domain, and the water region the $z \leqslant 0$ domain. The horizontal coordinates x and y are in the

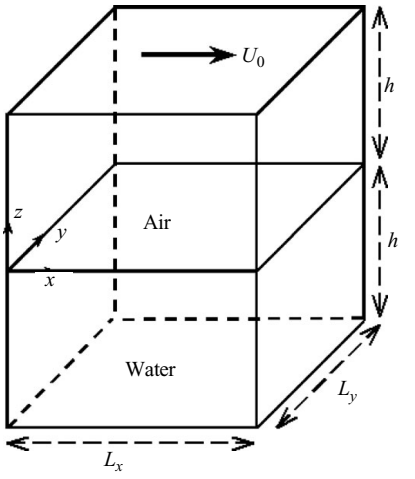

FIGURE 1. Numerical domain of two immiscible turbulent flows driven by velocity U_0 on a Cartesian coordinate. The interface of air and water is located at $z=0$. The size of air and water sub-domains is the same, $(L_x, L_y, h) = (6, 6, 1)h$.

streamwise and spanwise directions, respectively. The external forcing of the system is a constant velocity U_0 imposed at the upper boundary ($z=h$) in the air region, i.e. similar to a Couette flow. We set $U_0 = 3\,\mathrm{m\,s^{-1}}$ in this study.

2.2. *Governing equations*

The mass and momentum conservation equations for incompressible, Newtonian fluids of air and water with density ρ_ℓ and kinematic viscosity ν_ℓ are

$$\nabla \cdot \boldsymbol{u}_\ell = 0, \tag{2.1}$$

$$\frac{\partial \boldsymbol{u}_\ell}{\partial t} + \boldsymbol{u}_\ell \cdot \nabla u_\ell = -\frac{1}{\rho_\ell}\nabla p_\ell + \nu_\ell \nabla^2 u_\ell, \tag{2.2}$$

where the subscript ℓ denotes variables in air ($\ell = a$) or water ($\ell = w$), $\boldsymbol{u} = (u, v, w)$ are velocity components in streamwise, spanwise and vertical directions, respectively, and p_ℓ is the pressure.

The Poisson equation for p_ℓ is obtained by taking the divergence of (2.2) and using (2.1)

$$\frac{\partial^2 p_\ell}{\partial x^2} + \frac{\partial^2 p_\ell}{\partial y^2} + \frac{\partial^2 p_\ell}{\partial z^2} = \mathrm{H}_\ell, \tag{2.3}$$

where the source term H_ℓ is the divergence of the convective and diffusive terms in (2.2). The solution of (2.3) forces the continuity equation (2.1) to be satisfied at each time step.

2.3. *Boundary conditions*

The domains of the two immiscible fluids have six external boundaries and one internal deformable interface. For external boundaries, periodic conditions are assumed on the four sidewalls of the computational domain. At the top of the domain, $z=h$, a constant-velocity condition is applied as

$$u_a = U_0,\ v_a = 0,\ w_a = 0,\ \frac{\partial p_a}{\partial z} = 0. \tag{2.4}$$

At the lower bottom of the water region, $z=-h$, we impose free-slip boundary conditions

$$\frac{\partial u_w}{\partial z}=0,\ \frac{\partial v_w}{\partial z}=0,\ w_w=0,\ \frac{\partial p_w}{\partial z}=0, \tag{2.5}$$

to emulate an infinite depth.

For the deformable interface between the air and water, continuity of velocity, tangential and normal stresses is required across the boundary $z=\eta(x, y, t)$ (Wehausen & Laitone 1960). Without simplification, these requirements lead to complicated boundary conditions (see equations 3.2–3.6 in Wehausen & Laitone 1960). However, assuming small interfacial deformation where the ratio of wave amplitude to wavelength is smaller than 0.01, as in the initial wind-wave generation processes considered here, we can linearize the interfacial conditions (Tsai & Yue 1995), which yields boundary conditions satisfied at $z=0$ as follows:

$$u_a=u_w,\ v_a=v_w,\ w_a=w_w, \tag{2.6}$$

$$\mu_a\left(\frac{\partial u_a}{\partial z}+\frac{\partial w_a}{\partial x}\right)=\mu_w\left(\frac{\partial u_w}{\partial z}+\frac{\partial w_w}{\partial x}\right), \tag{2.7}$$

$$\mu_a\left(\frac{\partial v_a}{\partial z}+\frac{\partial w_a}{\partial y}\right)=\mu_w\left(\frac{\partial v_w}{\partial z}+\frac{\partial w_w}{\partial y}\right), \tag{2.8}$$

$$p_w-\rho_w g\eta+2\mu_w\left(\frac{\partial u_w}{\partial x}+\frac{\partial v_w}{\partial y}\right) - p_a+\rho_a g\eta-2\mu_a\left(\frac{\partial u_a}{\partial x}+\frac{\partial v_a}{\partial y}\right)=-\gamma\left(\frac{\partial^2\eta}{\partial x^2}+\frac{\partial^2\eta}{\partial y^2}\right), \tag{2.9}$$

where $\mu_a\equiv\rho_a\nu_a$ and $\mu_w\equiv\rho_w\nu_w$ are dynamic viscosities of air and water, and γ is the surface tension of the water interface. The linearized kinematical condition satisfied at $z=0$ is

$$\frac{\partial\eta}{\partial t}+\frac{\partial(u\eta)}{\partial x}+\frac{\partial(v\eta)}{\partial y}=w. \tag{2.10}$$

The use of a central-differencing scheme at the interface requires additional points (ghost points) below the interface for (u_a, v_a, w_a, p_a) and above the interface for (u_w, v_w, w_w, p_w) (figure 2). The (u_a, v_a, u_w, v_w) values at the ghost points are determined using the continuity conditions for velocity (2.6) and tangential stresses ((2.7) and (2.8)). (w_a, w_w) at the ghost points are determined by two additional conditions. (i) Applying the continuity equation (2.1) and the boundary conditions (2.6) at $z=0$ results in the condition

$$\frac{\partial w_a}{\partial z}=\frac{\partial w_w}{\partial z}. \tag{2.11}$$

(ii) A second condition is obtained by adding the x-derivative of (2.7) and the y-derivative of (2.8) (Chandrasekhar 1954), leading to

$$\mu_a\left(\frac{\partial^2 w_a}{\partial x^2}+\frac{\partial^2 w_a}{\partial y^2}-\frac{\partial^2 w_a}{\partial z^2}\right)=\mu_w\left(\frac{\partial^2 w_w}{\partial x^2}+\frac{\partial^2 w_w}{\partial y^2}-\frac{\partial^2 w_w}{\partial z^2}\right). \tag{2.12}$$

The pressure (p_a, p_w) at the ghost points is determined by applying the normal stress condition (2.9) and the continuity condition for the vertical velocity (2.6) to the

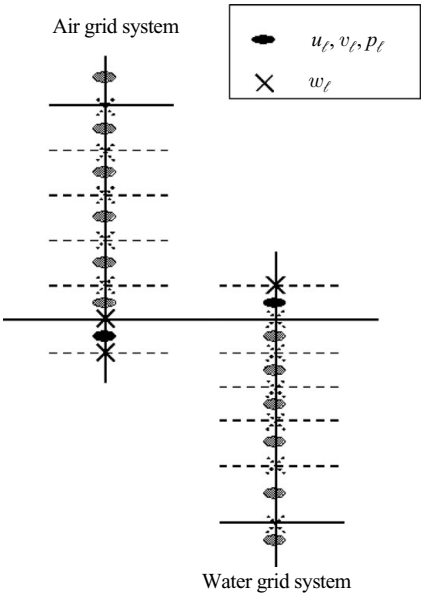

FIGURE 2. Location of velocity components and pressure on staggered grid systems for the mixed finite-differencing and pseudospectral scheme. Symbols with solid circle and cross are ghost points at the interface.

vertical component of the momentum equation at the interface, which results in

$$-\frac{1}{\rho_a}\frac{\partial p_a}{\partial z}-\frac{\partial(u_a w_a)}{\partial x}-\frac{\partial(v_a w_a)}{\partial y}-\frac{\partial(w_a w_a)}{\partial z}+\nu_a\left(\frac{\partial^2 w_a}{\partial x^2}+\frac{\partial^2 w_a}{\partial y^2}+\frac{\partial^2 w_a}{\partial z^2}\right)$$
$$=-\frac{1}{\rho_w}\frac{\partial p_w}{\partial z}-\frac{\partial(u_w w_w)}{\partial x}-\frac{\partial(v_w w_w)}{\partial y}-\frac{\partial(w_w w_w)}{\partial z}+\nu_w\left(\frac{\partial^2 w_w}{\partial x^2}+\frac{\partial^2 w_w}{\partial y^2}+\frac{\partial^2 w_w}{\partial z^2}\right). \tag{2.13}$$

2.4. *Numerical method*

The numerical method used to solve the system of equations (2.2) and (2.3) subject to the boundary conditions (2.4)–(2.10) is based on the scheme described by Tsai (1998) and Tsai *et al.* (2005). We use a staggered grid in the vertical as shown in figure 2 where the grids are stretched with finer resolution near the interface, as in Tsai *et al.* (2005). We use a pseudospectral method to evaluate x- and y-derivatives, second-order finite-difference scheme for z-derivatives, and a second-order Runge–Kutta method (Spalart, Moser & Rogers 1991) for time integration.

We use $(N_x, N_y, N_z) = (64, 64, 65)$ gridpoints in each of the air and water domains. The domain size in both x- and y-directions is 24 cm. In the water, the horizontal grid size in wall units is $\Delta x_w^+ = \Delta y_w^+ = \Delta y_w u_w^*/\nu_w = 11.25$, where the water friction velocity u_w^* is given in § 2.5. Near the interface, the stretched vertical grid adequately resolves the viscous layer. There are 14 grids in the near-surface region ($-z_w^+ \leqslant 10$). In the air domain, the corresponding non-dimensional horizontal spacings are $\Delta x_a^+ = \Delta y_a^+ = 21.4$, and there are 10 gridpoints within the region $z_a^+ \leqslant 10$ in the vertical direction near the interface.

As suggested by Moin & Mahesh (1998), the grid resolution requirements for the spectral method of boundary-layer flow in x (streamwise) and y (spanwise)

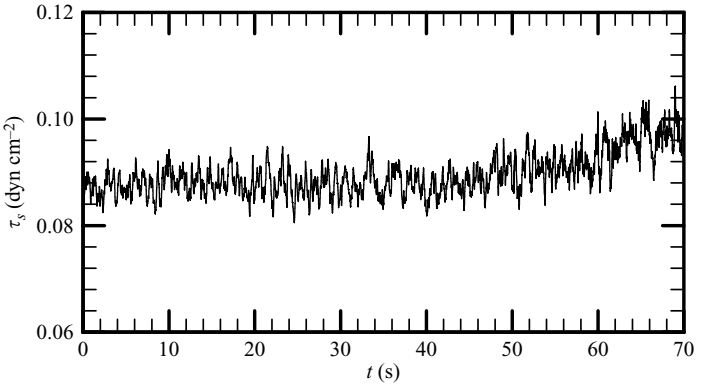

FIGURE 3. Time evolution of the mean wind stress τ_s at the interface.

and second-order central difference scheme in z are $(\Delta x, \Delta y, \Delta z) = (14.3, 4.8, 0.26)\xi$ where $\xi = (\nu_a^3/\varepsilon)^{1/4}$ is the Kolmogorov microscale, $\varepsilon \sim \upsilon^3/h$ is the dissipation rate and $\upsilon = (u_a'^2 + v_a'^2 + w_a^2)^{1/2}$ is the root-mean-square fluctuating speed. For our grid system, the Kolmogorov microscale is $\xi \sim 0.025$ cm, the horizontal spacing is 0.375 cm and the vertical spacing near the interface is about 0.01 cm. This spatial resolution is close to the requirements suggested by Moin & Mahesh (1998).

The non-dimensional time step is 0.005 where characteristic length and velocity are 4 cm and 300 cm s^{-1}, respectively.

2.5. *Initialization*

The simulation flow field is initiated in four steps. (i) We assign the mean velocity profile of the coupled air–water flow based on the analytical solution of laminar transient flow (Choy & Reible 2000) at the time when the mean velocity at the interface reaches 8 cm s^{-1}. (ii) We spin up the turbulence by adding small random perturbations in the air and water temperature fields to the buoyancy force in the w momentum equation. (The buoyancy force induces a quick spin-up to a turbulent state.) For this air–water coupled model, it takes about 120 large-eddy turnover time units ($U_0 t/h$) to spin up the turbulence. (iii) We turn off the buoyancy force in the w momentum equation and continue the spin-up simulation for another 2400 large-eddy turnover time units to reach a pure shear-driven state. The criterion for established pure shear-driven flow is determined by comparing the near-surface velocity variances in the air and water domains to the shear turbulent flow above a flat boundary reported in Sullivan *et al.* (2000) and the shear-driven turbulent water flow in Tsai *et al.* (2005). Finally, we start our simulation from this fully developed shear-driven turbulent flow by allowing the flat interface to deform. All results shown below are from this final stage.

Figure 3 shows the time evolution of the mean shear stress τ_s at the interface after the interface is allowed to evolve. For the time interval $t < 50$ s, the mean interfacial stress τ_s remains at a nearly constant value of 0.089 dyn cm^{-2}, implying that our simulation has reached a statistically quasi-steady state in response to the wind forcing. The associated friction velocities in the air and water are $u_a^* = \sqrt{\tau_s/\rho_a} \approx 8.56$ cm s^{-1} and $u_w^* = \sqrt{\tau_s/\rho_w} \approx 0.3$ cm s^{-1}, respectively. The ratio of u_a^*/U_0 is hence about 0.03. For $t > 50$ s, the mean interfacial stress smoothly increases owing to the growth of surface waves. We discuss the properties of the generated waves in § 6.

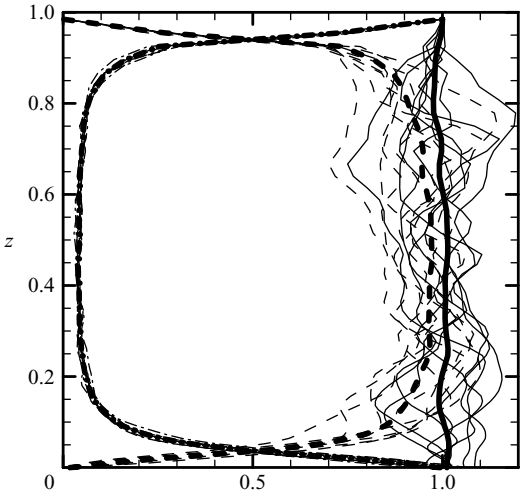

FIGURE 4. Vertical profiles of dimensionless mean vertical turbulent flux $-\langle u'_a w'_a\rangle/(u^*_a)^2$ (thick dashed line), viscous flux $(\nu_a/u^*_a h)\partial U_a/\partial z$ (thick dash-dotted line), and their sum (thick solid line) in the air. The thin lines represent these terms at various time instances from 50 to 70 s, while the thick lines are their averages.

The total u momentum flux in the air is

$$\nu_a \frac{\partial U_a}{\partial z} - \langle u'_a w'_a\rangle = u^*_a. \tag{2.14}$$

Figure 4 shows the vertical distributions of viscous, turbulence, and total momentum flux. As required for a Couette flow under a steady condition, the total mean vertical momentum flux is nearly constant with height.

The bulk Reynolds number of the air flow ($Re_a \equiv U_0 h/\nu_a$) is about 8000. This value is the same as that in the turbulent Couette flow simulation of Sullivan *et al.* (2000). The simulated turbulence, therefore, is considered to be fully developed. The associated wall Reynolds number ($Re^*_a \equiv u^*_a h/2\nu_a$) is about 115. Our wall Reynolds number is about 12 % less than that of Sullivan *et al.* (2000). In the water, the bulk Reynolds number ($Re_w \equiv U_s h/\nu_w$) is about 2000, where $U_s \approx 10\,\mathrm{cm\,s^{-1}}$ is the mean velocity at the interface. The corresponding wall Reynolds number ($Re^*_w \equiv u^*_w h/2\nu_w$) is about 60, which is comparable to that in the simulations reported by Lombardi *et al.* (1996) and Tsai *et al.* (2005).

3. Flow visualization

3.1. *Waves and streaks*

Waves and streaks are frequently observed phenomena at the air–water interface; they are also found in our numerical simulations. Figure 5 shows contour distributions of the interface elevation $\eta(x, y, t)$ and the streamwise velocity $u_w(x, y, z=0, t)$ at three representative time instances $t = 2.6$, 16 and 66 s. The results show that the surface waves grow in time in our simulation (figure 5*a–c*). High-speed streaks are observed before the initiation of surface waves (figure 5*d*, *e*). When the wave motion is weak, the structure of the high-speed streaks (figure 5*d*) is similar to that observed by Tsai *et al.* (2005) in which a stress-driven free-surface turbulent shear flow is considered. Low-speed streaks in the air flow near the interface (figure 6*a*) are also

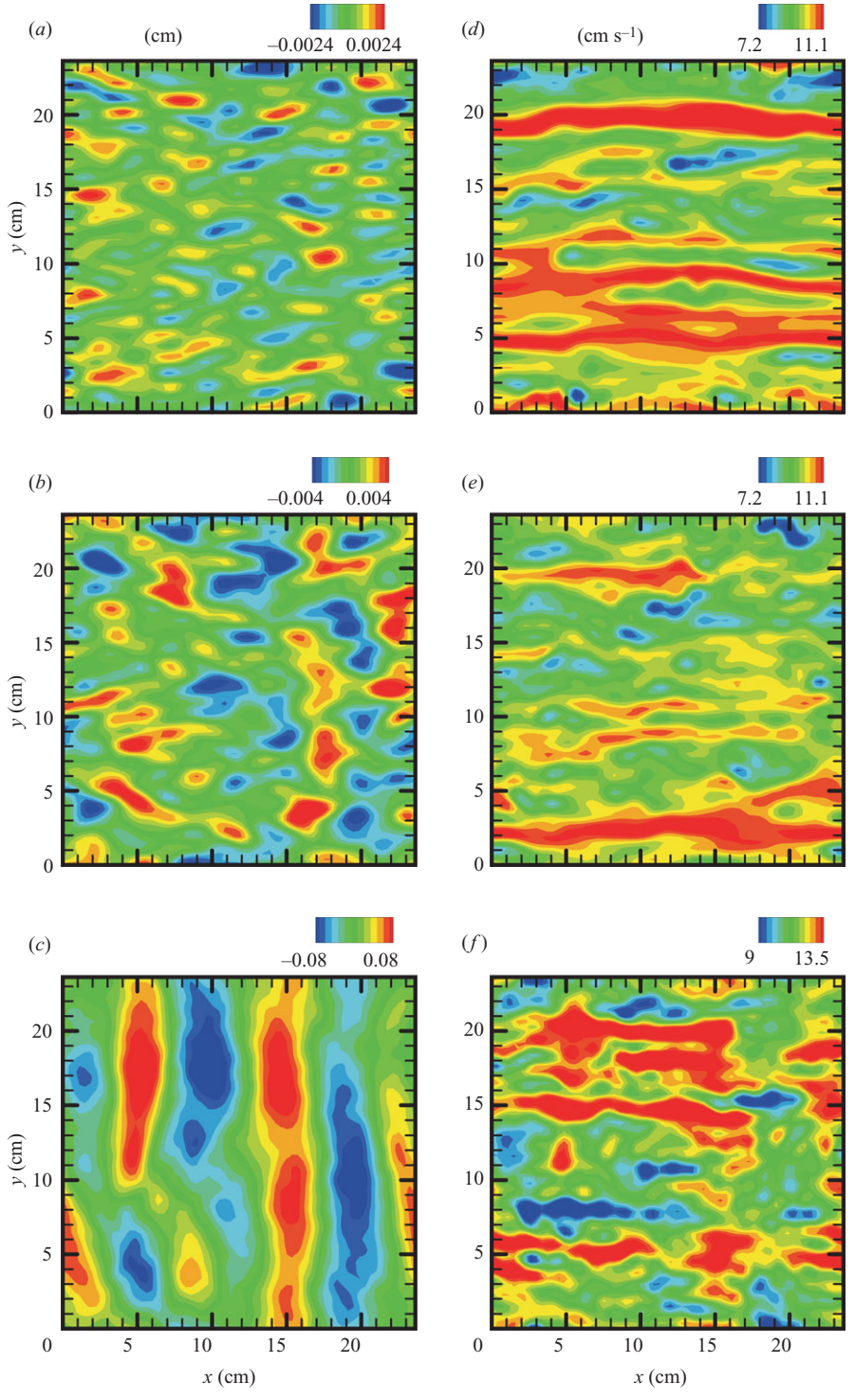

FIGURE 5. Snapshots of the instantaneous water surface elevation η (a–c) and streamwise velocity u at the interface (d–f) at time $t = 2.6$ s, 16 s and 66 s (from top to bottom), respectively.

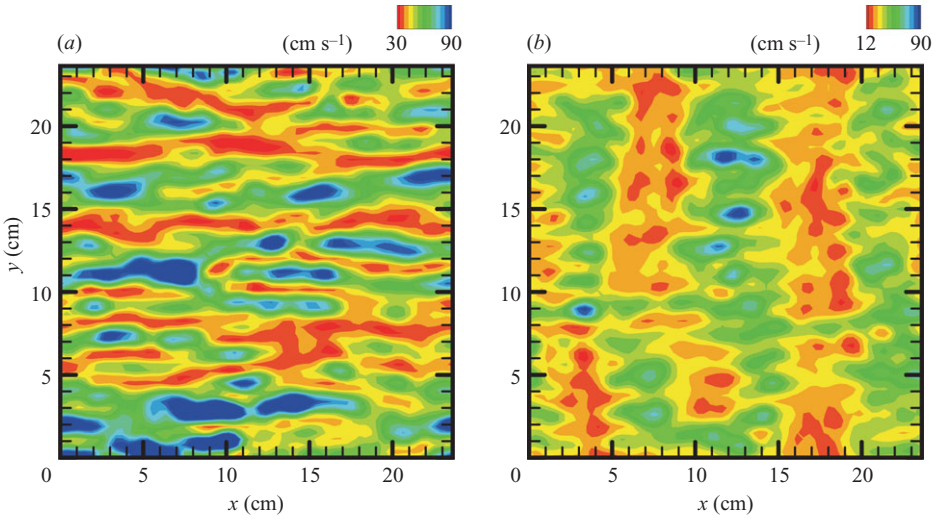

FIGURE 6. Snapshots of the instantaneous streamwise velocity u_a within the viscous sublayer of the air domain at time (*a*) $t = 2.6$ s and (*b*) 66 s.

observed. The low-speed streaky structure is similar to that commonly observed in a turbulent boundary layer next to a stationary no-slip boundary (e.g. Kim, Moin & Moser 1987). When the wave motion becomes significant, the streaky velocity pattern shown in figure 5(*e*) is disrupted and now figure 5(*f*) reveals a waveform pattern that is embedded upon the streaky pattern, that is, the velocity now has relatively larger values along the wave crests around $x = 5$, 15 and 23 cm. Similarly, the streamwise velocity within the viscous sublayer on the air side (figure 6*b*) is also re-organized into waveform. However, the wave-induced motions in the air have a phase shift with the surface waves so figure 6(*b*) shows relatively weaker winds along $x = 7$ cm and 17 cm.

Figure 7 shows isosurfaces of the vertical velocity in the water at two representative time instances before and after the generation of the surface waves. When surface waves are weak, as shown in figure 7(*a*), the flow is shear dominated and the distributions of ejections and sweeps are irregular. However, when the flow becomes wave dominated, the vertical velocity distributions align with the waves (figure 7*b*).

In the air side, the wave effect on the air velocity field is not as significant as that in the water and confined to within the viscous sublayer as shown in figure 8(*a–c*). However, for the air pressure field (figure 8*d–f*), the wave effect can extend outside the viscous sublayer when the interface is wave dominated. These different responses of the velocity and the pressure fields to the surface waves were also observed by Sullivan *et al.* (2000).

3.2. *Pressure and stress fields*

Figure 9 shows two representative distributions of the fluctuating air and water pressures, p'_a and p'_w, at the interface, and the distribution of surface-wave elevations. At the early stage when surface waves are weak, pressure fluctuations in the air do not show any pattern similar to the surface-wave elevations (comparing figures 9*a* with 9*b*), but comparing figures 9(*c*) and 9(*b*) we can see a similar pattern between the pressure fluctuations in the water and the surface-wave elevations even at $t = 16$ s. This suggests that in the early stage of wind-wave generation, pressure fluctuations in the water are driven almost passively by surface waves, and the turbulence in the water may not play an important role in generating waves. In § 8, a numerical experiment

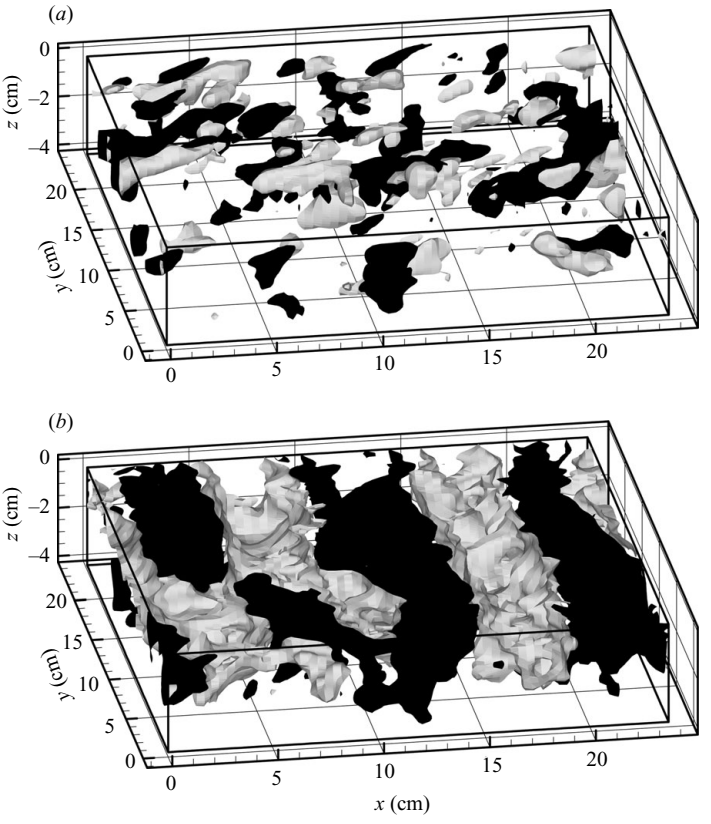

FIGURE 7. Representative iso-surfaces of vertical velocity in the water at time (*a*) $t = 2.6$ s and (*b*) 66 s. Black and grey iso-surfaces show vertical velocity speed of $-1.5\,\mathrm{cm\,s^{-1}}$ and $+1.5\,\mathrm{cm\,s^{-1}}$, respectively.

is designed to test the impact of water turbulence on wind-wave generation processes. When wave motions dominate (figure 9*d–f*), we observe that both the pattern of pressure fields (figure 9*d*, *f*) are similar to the waveform. At this stage, the air pressure fluctuations show a slight phase shift relative to the surface waves, and the region of maximum (minimum) pressure occurs on the backward (forward) face of the surface wave near the crest (trough), as observed by Sullivan *et al.* (2000). Belcher, Newley & Hunt (1993) term this phenomenon non-separated sheltering. Also, the pressure fluctuations in the air (figure 9*d*) are less regular than those in the water (figure 9*f*), implying that the pressure fluctuations in the air are more turbulence induced than wave induced.

Figure 10 shows shear stress fluctuations at the interface at early (figure 10*a*) and late (figure 10*b*) stages of wave growth. Similar to the pressure field in the air, the shear stress field reveals a wave-induced component only when the waves become strong. The wave-induced shear-stress fluctuations also exhibit a phase shift relative to the surface-wave elevations.

The wave effect on the pressure fields in the vertical direction can also be seen in the vertical distributions of pressure fluctuations at $t = 16$ s (figure 11*a–c*) and 66 s (figure 11*d–f*). At $t = 66$ s, pressure fluctuations in the air and water are influenced by waves, and the wave effect extends outside the viscous sublayer. At $t = 16$ s, pressure

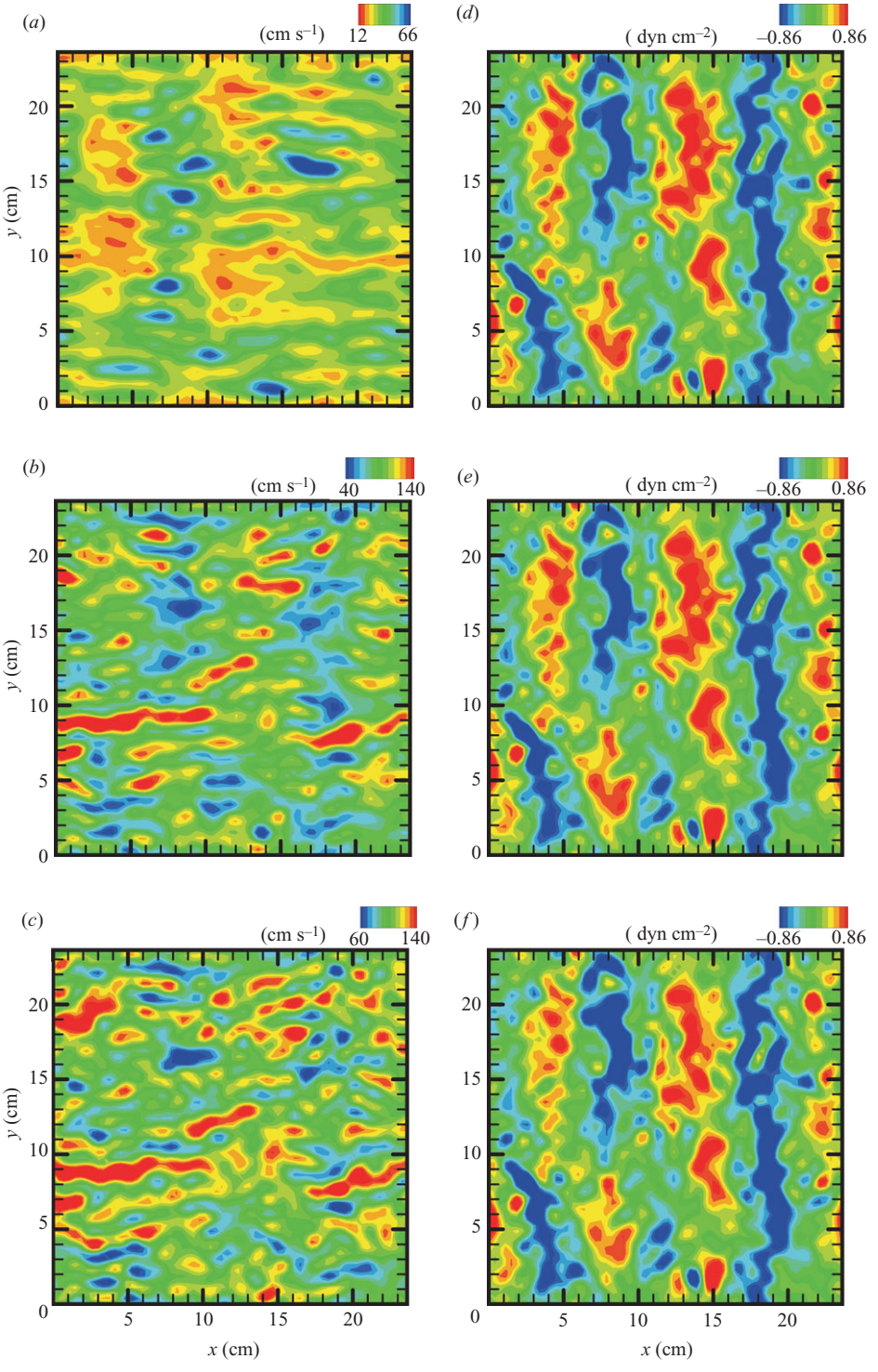

FIGURE 8. Snapshots of the instantaneous streamwise velocity (*a–c*) and pressure fluctuations (*d–f*) of the air flow in (x, y)-planes at $t = 66$ s at three different heights. (*a*), (*d*) are within the viscous sublayer $z = 0.045$ cm, (*b*), (*e*) are in the matched layer $z = 0.23$ cm, and (*c*), (*f*) are in the inertial sublayer $z = 0.37$ cm.

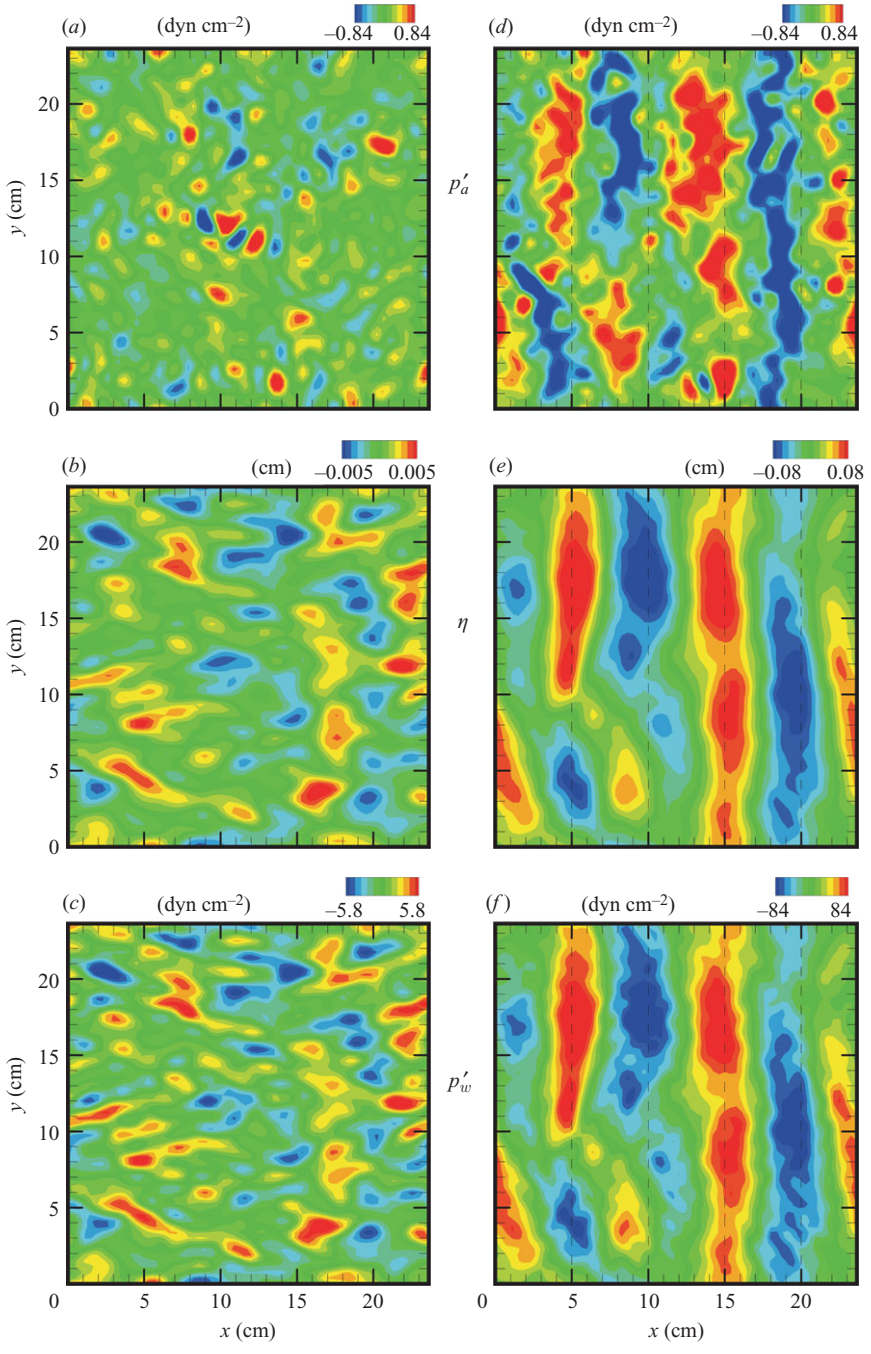

FIGURE 9. Snapshots of the instantaneous pressure fluctuations in the air p'_a (a, d) and water p'_w (c, f), and water surface elevation η (b, e) on the interface at time $(a–c)$ $t = 16$ s and $(d–f)$ 66 s.

fluctuations in the air show no similarity to the surface wave motions, but the pressure fluctuations in the water already follow the wave pattern. Simultaneous animations of η and p'_a show that at early time, pressure fluctuations in the air usually sweep

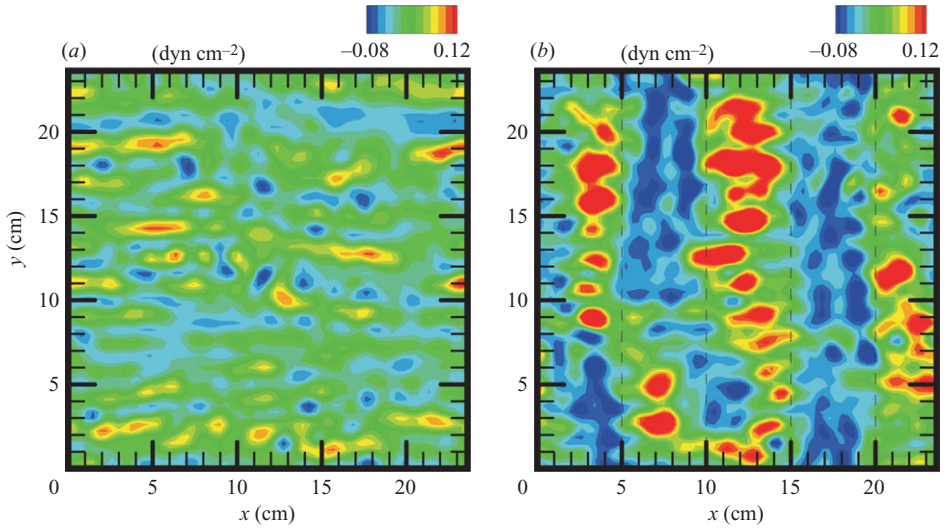

FIGURE 10. Snapshots of the instantaneous shear stress fluctuations τ_s' at the interface at time (*a*) $t = 16$ s and (*b*) 66 s.

over the water surface with varying speeds higher than the phase velocity of the wave motions, but at late time, the convection speed of p_a' is the same as the phase velocity of the surface waves. This suggests different wave-generation processes at early and late times. We will discuss this in more detail in § 7.

4. Characteristics of the surface waves

Figure 12 shows the wavenumber spectra of surface elevation at $t = 2.6$, 16 and 66 s. At the beginning of the simulation ($t = 2.6$ s) when the water-surface elevation is randomly distributed (figure 5*a*), the spectrum shows no significant energy in the low-wavenumber range (figure 12*a*). As waves begin to form at $t = 16$ s (figure 5*b*), the wave energy is more or less evenly distributed at certain selected wave components (figure 12*b*). When waves become strong at $t = 66$ s (figure 5*c*), wave energy is concentrated in a few small-wavenumber components (figure 12*c*). Table 1 gives the five largest energy-containing components at early ($t \sim 16$ s) and late ($t \sim 66$ s) stages. At early time, the fraction of energy in each component is low and rather evenly distributed. At a later stage, about 80 % of wave energy is possessed by three wave components. These fastest growing waves are $(k_x, k_y) = (0.78, 0)$, $(0.78, 0.26)$ and $(0.52, 0)\,\mathrm{cm}^{-1}$. Their associated wavelengths are in the range of 8 to 12 cm, close to those found by Kahma & Donelan (1988) in their laboratory experiment. The wavenumber–frequency spectrum of the surface-wave elevations are plotted in figure 13 for the time interval $t = 66$–66.5 s. It shows that the frequency of the most energetic wave component $(k_x, k_y) = (0.78, 0)\,\mathrm{cm}^{-1}$ is $36.9\,\mathrm{s}^{-1}$, which agrees with the linear dispersion relation for a propagating gravity wave (dashed line in figure 13).

We compare the wavelength found here and those found in previous experimental studies as follows. Caulliez & Collard's (1999) experiments show that wave motions have five distinct regimes depending on wavelength and steepness in the wind-wave generation processes. They split these five regimes into two categories according to the wind speed: one for low wind speeds ($U < 4\,\mathrm{m\,s}^{-1}$) and the other for higher wind speed ($U > 4\,\mathrm{m\,s}^{-1}$). For the first category at low wind speeds, the wavelengths of

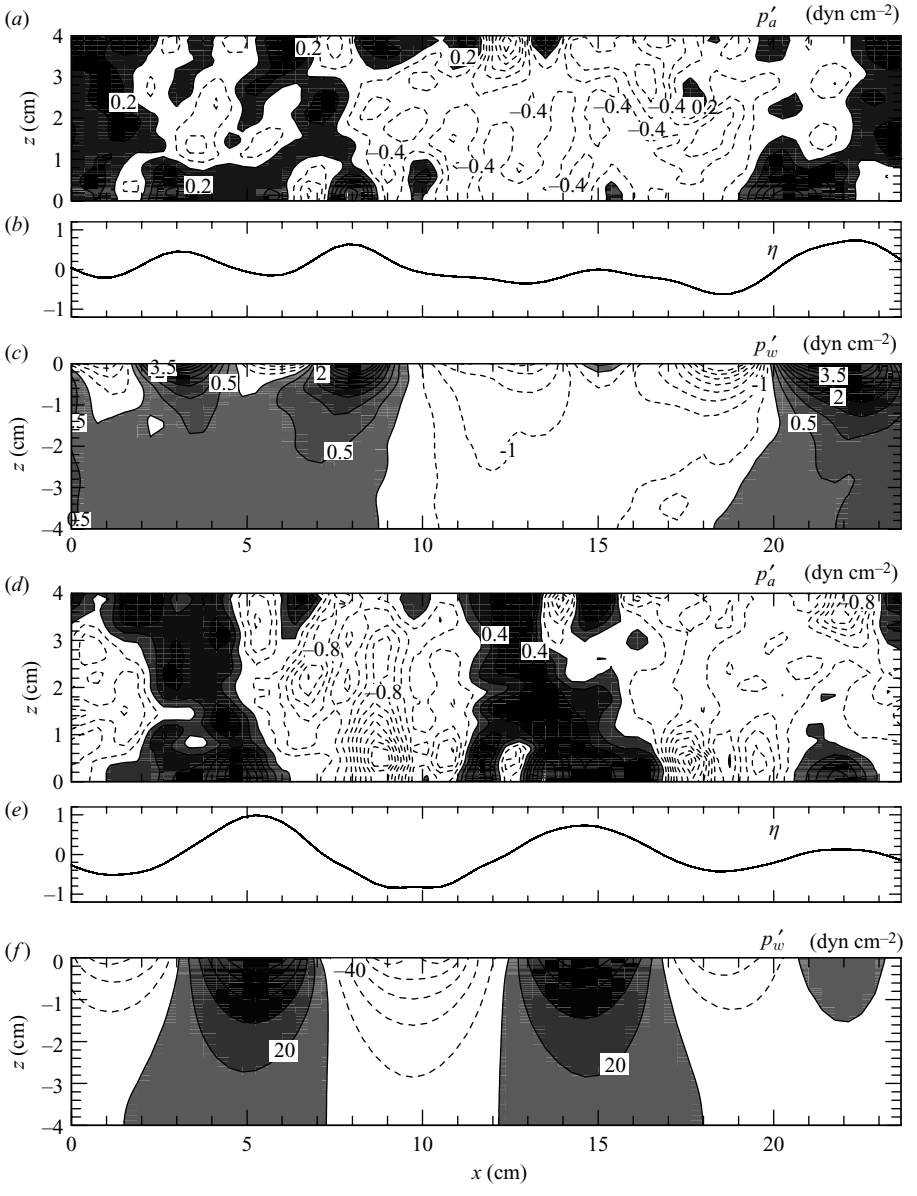

FIGURE 11. Snapshots of instantaneous pressure fluctuations in the air p'_a and water p'_w in an (x, z)-plane and the associated water surface elevation η at time (*a–c*) $t = 16$ s and (*d–f*) 66 s. The cross-section is located at $y = 18$ cm in figure 9. η is normalized by its maximum value at this time.

initial waves (the first visible waves) are within the range of 4 to 10 cm and no waves smaller than 4 cm can be generated. Many kinds of wave pattern can be found in the second category. One of them is the longer gravity waves superimposed by short-crested capillary waves with wavelengths usually between 0.5 and 1 cm. Plate, Chang & Hidy (1969) also observed these two categories of waves in their wind-wave tank when the steady wind is gradually increased in speed. They interpreted this phenomenon as 'The first waves, near critical wind speeds, are smooth undulations,

	Wavenumber $\kappa = (k_x, k_y)$ (cm^{-1})	$\Phi(k_x, k_y)/\langle\eta^2\rangle$
$t \sim 16$ s	(1.0, 1.0)	6.5 %
	(1.0, 0.0)	6.1 %
	(0.26, 1.0)	5.9 %
	(0.52, 0.52)	5.0 %
	(0.52, 0.0)	4.7 %
$t \sim 66$ s	(0.78, 0.0)	28.0 %
	(0.78, 0.26)	24.7 %
	(0.52, 0.0)	24.5 %
	(0.52, 0.26)	7.2 %
	(1.0, 0.26)	3.3 %

TABLE 1. Dominant waves and the percentage of each wave energy at early ($t \sim 16$ s) and late ($t \sim 66$ s) stages for the control case. Note that the dominant waves at these two stages are different. $\Phi(k_x, k_y)$ is the wave energy of the selected wave component.

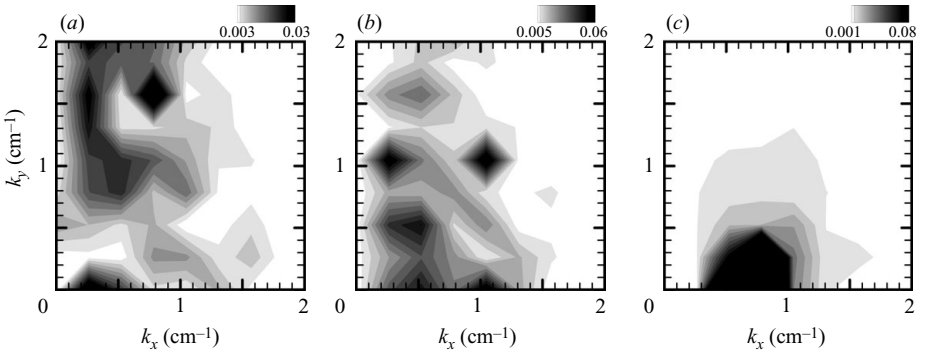

FIGURE 12. Wavenumber spectra of water surface elevation $\hat{\eta}(k_x, k_y)$ (normalized by its total energy) at time (*a*) $t = 2.6$ s, (*b*) 16 s and (*c*) 66 s. Note that the maximum contour level in (*c*) is higher than that in (*a*) and (*b*). The resolution of wavenumber spectra in x- and y-directions is about 0.26 cm^{-1}.

two-dimensional in appearance, which are oriented with crest nearly perpendicular to the direction of flow. As the wind speed increases, the water surface becomes somewhat more ruffled. Short-crested capillary ripples are superimposed over the first undulations and a rhombic wave pattern develops.' Based on these two studies, we classify waves found from other experiments as follows.

Kahma & Donelan's (1988) experiments at low wind speeds (lower than 4 m s^{-1}) show that wavelength of the fastest growing waves is about 7–10 cm, and their frequency spectrum has only one energy peak at low frequency; no bi-modal shape is found. These waves belong to Caulliez & Collard's (1999) first category.

Veron & Melville's (2001) experiment exhibits a bi-modal shape in the saturation spectrum at the wind speed of 5 m s^{-1}; this characteristic is caused by parasitic capillary waves ($\lambda \sim 0.78$ cm) riding on the longer gravity waves ($\lambda \sim 12.5$ cm), and hence belongs to the second category classified by Caulliez & Collard (1999). Kawai (1979) set up the experiment at high wind speeds (wind speeds larger than 4 m s^{-1}) and found that the wavelengths of initial wavelets are less than 4 cm, which also belong to the second category according to Caulliez & Collard. Larson & Wright (1975) used microwave backscatter to measure the growth rates of wind-induced water waves at

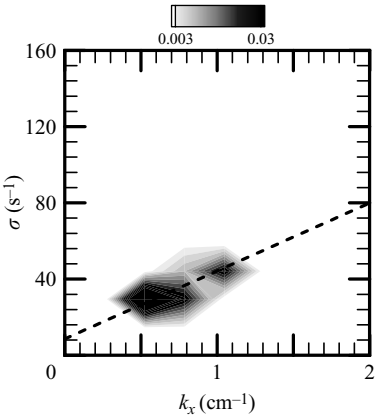

FIGURE 13. Wavenumber–frequency spectrum of the water surface elevation $\hat{\eta}(k_x, \sigma)$ (normalized by its total energy) at time interval $t = 66$–66.5 s for $k_y = 0$. The dashed line represents the linear dispersion relation $\sigma/k_x = U_s + \sqrt{g/k_x}$ where $U_s = 12\,\mathrm{cm\,s^{-1}}$ is the mean surface current. Even though the deep-water wave approximation is not suitable for the wave component of $k_x = 0.52\,\mathrm{cm^{-1}}$, we approximated the dispersion relation $\sigma^2 = gk \tanh kh$ to $\sigma^2 = gk$ for this wave component; the error due to this approximation is within 5 %. The resolutions of wavenumber and frequency are $0.26\,\mathrm{cm^{-1}}$ and $14.8\,\mathrm{s^{-1}}$, respectively.

high wind speeds in a laboratory wave tank. Since longer waves grew more slowly, they neglected the longer waves in the initial stages of Bragg wave growth and focused their study on waves at wavelengths of 0.7–7 cm. We also classify these smaller waves riding on longer waves in the second category of Caulliez & Collard (1999).

The waves reported in this paper have wavelengths in the range of 8–12 cm, and show no bi-modal shape in the energy spectra. Thus, our waves belong to Caulliez & Collard's (1999) first wave category. However, we did observe some wavelengths less than 4 cm in our simulation when the surface wave slope became steep and the nonlinear effect began to dominate the wave growth process. Figure 14 shows the wave slope and curvature of surface waves at time $t = 56$ and 69 s that reveal the existence of small ripples near time $t = 69$ s. However, because of the use of a linearlized interfacial boundary condition, we restrict our discussion to the simulation before the nonlinear effect becomes significant.

5. Wave effect on mean velocity profiles and turbulence intensities

Surface waves at the air–sea interface have significant effects on the mean velocity profiles of air and water flows (Sullivan *et al.* 2000; Cheung & Street 1988; Howe *et al.* 1982). To examine the wave effect on the mean velocity profiles, we compare the air and water mean velocity profiles in our simulation with the two-layer velocity profile of a wall turbulent boundary layer

$$U^+ = z^+, \tag{5.1}$$

within the viscous sublayer, and

$$U^+ = \frac{1}{\kappa} \ln z^+ + b \equiv \frac{1}{\kappa} \ln \frac{z^+}{z_0^+}, \tag{5.2}$$

in the inertial layer, where κ is the von Kármán constant, b is a constant related to the surface roughness length z_0^+, and $z_0^+ = e^{-\kappa b}$. The non-dimensional wall coordinate

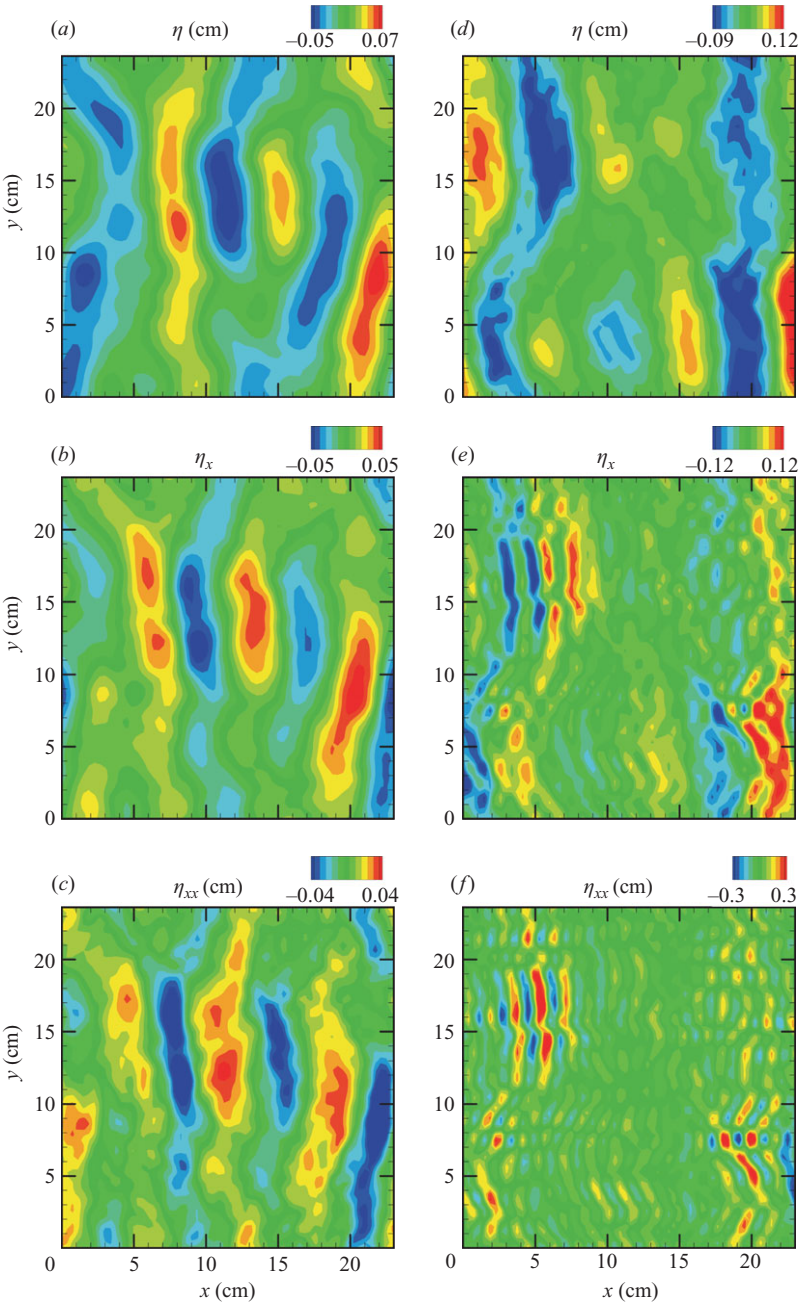

FIGURE 14. Snapshots of the instantaneous water surface elevation η (a, d), wave slope η_x (x derivatives; b, e) and wave curvature in x (c, f) at time $(a$–$c)$ $t = 56$ s and $(d$–$f)$ 69 s, respectively.

z^+ and velocity U^+ are defined as $z_a u_a^*/\nu_a$ and $(U_a - U_s)/u_a^*$ in the air and $-z_w u_w^*/\nu_w$ and $(U_s - U_w)/u_w^*$ in the water, respectively. U_s is the mean velocity at the interface, and U_a and U_w are the mean velocities in the air and in the water, respectively.

We compute the mean velocities by averaging the flow field in horizontal planes at each time, and plot the time variation of these mean velocities in figure 15, along

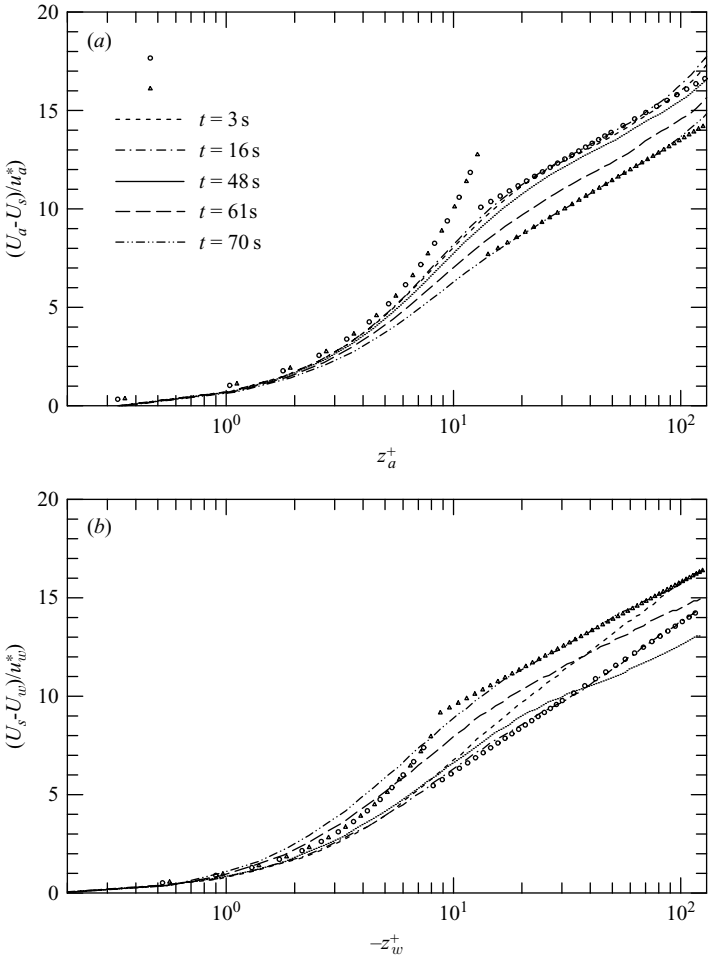

FIGURE 15. Mean profiles of the streamwise velocity of (*a*) the air and (*b*) water. The symbol ○, matched linear-logarithmic profiles at $t = 16$ s; △, $t = 70$ s. The log-law constants used to collapse the profiles (κ, z_0^+) are (0.34, 0.31) and (0.33, 0.84) in the air and (κ, z_0^+) are (0.3, 1.55) and (0.37, 0.3) in the water at time $t = 16$ s and 70 s, respectively.

with the theoretical profiles. Figure 15(*a*) shows that the simulated mean velocity profiles in the air compare well with the theoretical two-layer velocity profile. When surface waves are small ($t < 50$ s), the mean velocity profiles fit the same linear-logarithmic profile. However, when surface waves become significant ($t > 50$ s), wave motions change the mean velocity profiles, a systematic downward shift with time. This downward shift in the air velocity profile is equivalent to an increase in surface roughness z_0^+ (figure 17*f*), as described in Sullivan, McWilliams & Melville (2004), implying the enhancement of surface drag due to waves. The surface roughness z_0^+ is nearly constant ~ 0.3 when $t < 50$ s and increases to about 0.95 when $t \sim 70$ s. The associated von Kármán constant used to fit the logarithmic profile is about 0.33 at all time. Figure 15(*b*) shows the simulated mean velocity profiles and their associated two-layer velocity profiles in the water. Not all profiles show the logarithmic distribution and the von Kármán constant κ is changing with time, $0.22 < \kappa < 0.36$ when $t < 24$ s and $0.36 < \kappa < 0.44$ when $t > 24$ s. (At $t = 3$ s, the flow in the water may be too viscous

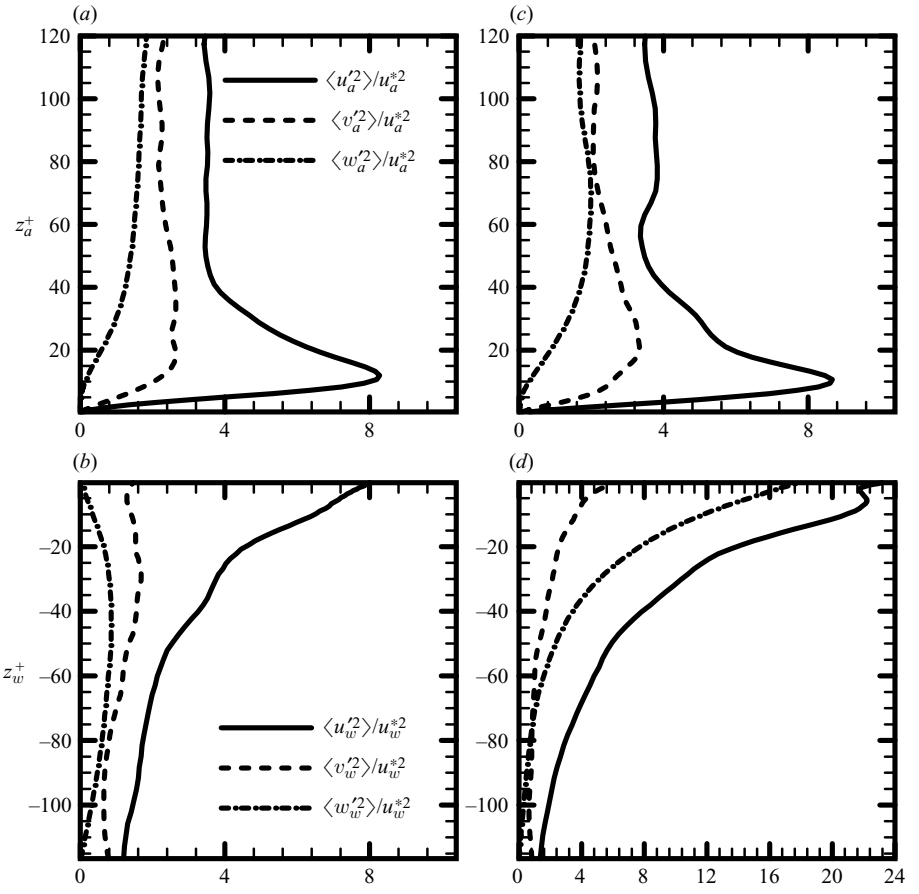

FIGURE 16. Vertical distributions of the normalized turbulent velocity variances of the air (a, c) and of the water (b, d) at (a, b) early ($t = 16$ s) and (c, d) later ($t = 66$ s) stages. Note that the horizontal scales in (b) and (d) are different.

as the mean wind profile is rather linear throughout.) The mean velocity profiles do not undergo a systematic downward shift with time as in the air.

The wave effect on the turbulent velocity variances is also different in air and water. Figure 16 shows the turbulent velocity variances at two stages: $t = 16$ s when turbulence dominates (figure 16a, b); and $t = 66$ s when waves dominate (figure 16c, d). In the air, the vertical distributions of the velocity variances (normalized by the surface friction velocity) $\langle u_i'^2\rangle(z)/(u_a^*)^2$ are in close agreement with wall-bounded shear turbulent flows (Kim *et al.* 1987; Aydin & Leutheusser 1991; Papavassiliou & Hanratty 1997; Sullivan *et al.* 2000). There is no significant change between turbulence and wave-dominated stages. In the water, our profiles at $t = 16$ s agree with the stress-driven turbulent flow simulated by Tsai *et al.* (2005). However, at the stage when waves become significant, the velocity variances in the water are strongly affected by waves, particularly the w-component. The horizontal-velocity variances near the interface also increase significantly owing to waves. Such an enhancement in the near-surface turbulent velocity variances is attributed to the orbital motions of the generated surface waves.

6. Wave growth types

Previous theoretical studies suggest that wave growth processes can be separated into linear and exponential growth stages and that the forcing mechanisms may involve either turbulence-induced or wave-induced pressure and stress fluctuations. The consensus is that in the linear growth stage, the wave-induced effects are ineffective since wave motions are weak and thus turbulence plays a major role in generating waves. In the exponential growth stage, wave-induced fluctuations of pressure and stress dominate and result in a feedback mechanism to grow waves quickly. In this study, we examine the wave growth processes in our simulated flow by classifying the simulation into linear and exponential wave-growth stages using four features as follows.

(i) The behaviour of pressure and shear stress fluctuations in the air is different at early and later stages as described in § 3.2; they are turbulence dominated at the early stage and wave dominated at the later stage. (ii) The time evolution of the root-mean-square of water-surface elevation $\langle \eta^2 \rangle^{1/2}$ (figure 17*a*) clearly shows slow growth before $t \sim 40$ s and fast growth after $t \sim 40$ s. Other statistical quantities, such as the mean surface current U_s, the root-mean-square of pressure fluctuations $\langle p_a'^2 \rangle^{1/2}$, the root-mean-square of the interfacial shear-stress fluctuations $\langle \tau_s'^2 \rangle^{1/2}$, the form stress D_p and the surface roughness z_0^+ (shown in figure 17*b–f*) also behave differently during early and late stages of the wave growth. They are nearly constant before $t \sim 40$ s and then increase sharply with time. (iii) The individual wave components of the fastest growing modes given in table 1 also reveal linear and exponential growth as shown in figure 18 where the time evolutions of the wave amplitudes of the five fastest-growing waves in linear coordinates for $t < 16$ s are shown in figure 18(*a*), and the three fastest-growing waves in exponential coordinates for $40 < t < 68$ s in figure 18(*b*). They clearly reveal trends of linear and exponential growth for each wave mode at the early and later stages, respectively. (iv) Each wave component of the form stress also shows different behaviour at the early and later stages of wave growth. Here, we define the dimensional form stress per unit area, D_p, of each wave component as

$$D_p = \frac{1}{L_x L_y} \int_0^{L_y} \int_0^{L_x} p_a' \left(\frac{\partial \eta}{\partial x} + \frac{\partial \eta}{\partial y} \right) \mathrm{d}x \, \mathrm{d}y. \tag{6.1}$$

Again we plot the time evolution of D_p of the five largest waves in linear coordinates for $t < 16$ s in figure 19(*a*) and the largest three waves in exponential coordinates during $40 < t < 68$ s in figure 19(*b*). The form stress is nearly zero when $t < 16$ s, but increases exponentially with time when $t > 40$ s. Because the form stress oscillates rapidly in the transition regime between 40 s and 50 s, we choose $0 < t < 16$ s as the linear growth stage and $50 < t < 70$ s as the exponential growth stage.

7. Comparison with wind-wave generation theories and measurements

7.1. *Linear growth stage*

Phillips (1957) proposed a theoretical model for wave generation and argued that the turbulence-induced pressure fluctuations in the air are responsible for the birth and early growth of waves. His theoretical model predicts that most of the growth of waves occurs in the principal stage of development and the following expression for linear growth:

$$\langle \xi^2 \rangle \sim \frac{\langle p_a'^2 \rangle}{2\sqrt{2} \rho_w^2 g U_c} t, \tag{7.1}$$

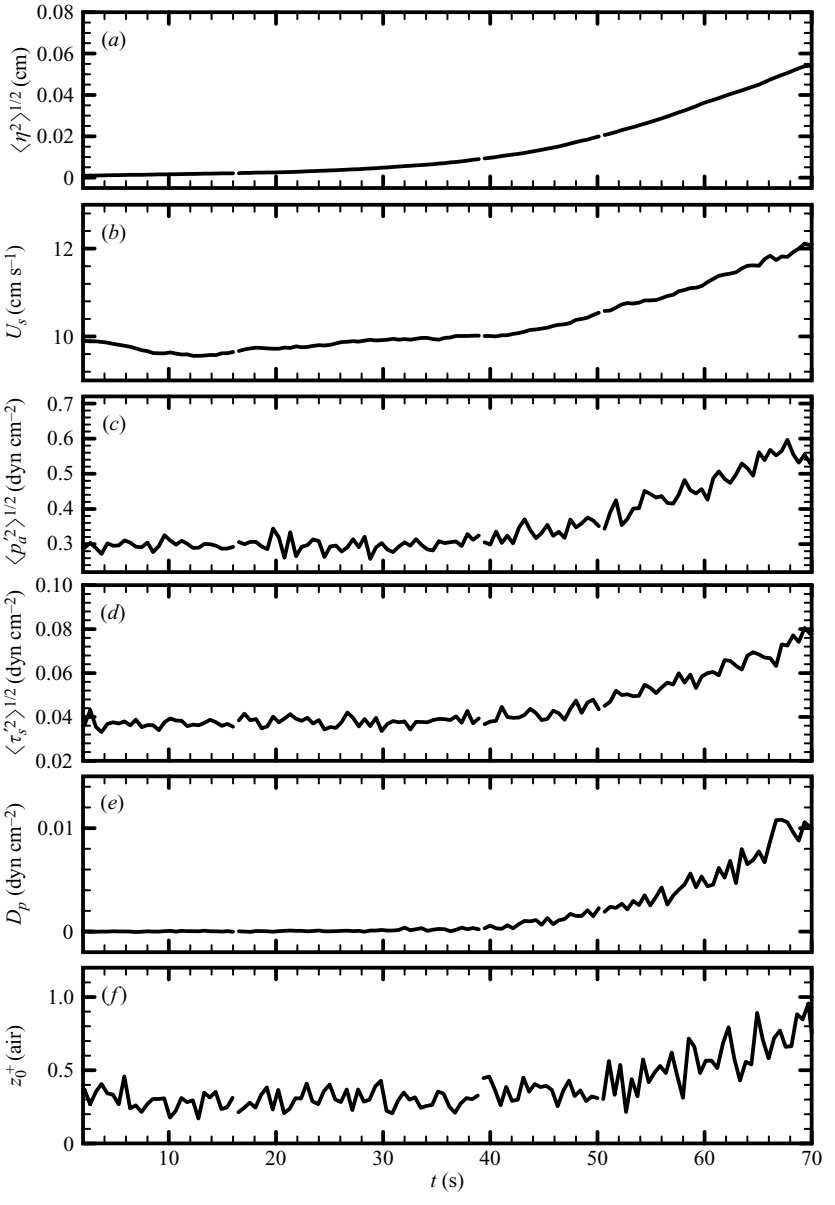

FIGURE 17. Time evolution of interfacial parameters: (*a*) root-mean-square of water surface elevation $\langle \eta^2 \rangle^{1/2}$, (*b*) mean surface current U_s, (*c*) root-mean-square of pressure fluctuations $\langle p_a'^2 \rangle^{1/2}$, (*d*) root-mean-square of shear stress fluctuations $\langle \tau_s'^2 \rangle^{1/2}$, (*e*) form stress D_p and (*f*) surface roughness length z_0^+ of the air.

where $\langle \xi^2 \rangle$ is the mean square water-surface elevation, $\langle p_a'^2 \rangle$ the mean square turbulent pressure of the air at $z = 0$, and U_c the convection speed of the near-surface pressure fluctuations.

For the application of (7.1), Phillips (1957) stated that U_c is close to the mean wind velocity at a certain height above the water surface; moreover, he proposed the following relation between air friction velocity and convection speed

$$U_c \sim 18 u_a^*, \tag{7.2}$$

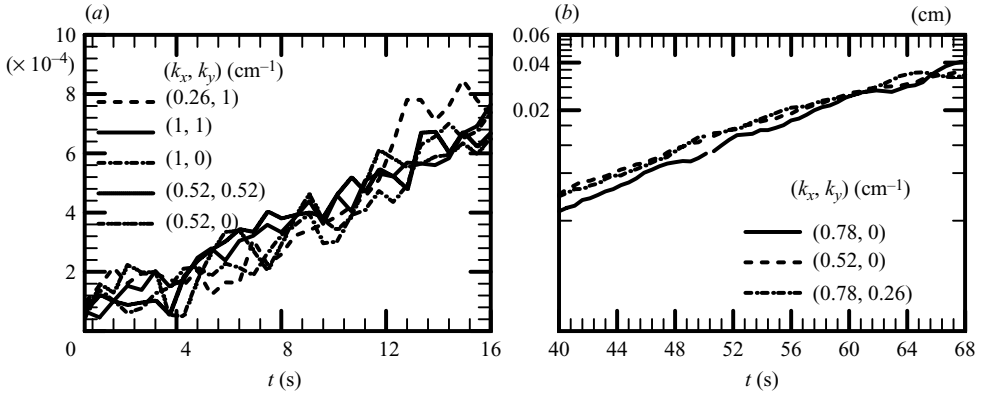

FIGURE 18. Time evolutions of wave amplitudes $\hat{\eta}(k_x, k_y)$ of (*a*) the five fastest growth waves at early stage, and (*b*) the three fastest growth waves at late stage. Note that we use a linear coordinate for (*a*) but an exponential coordinate for (*b*).

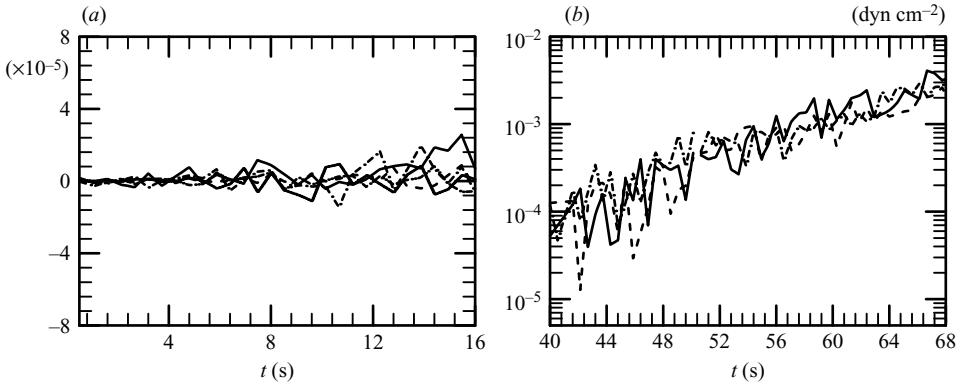

FIGURE 19. Time evolution of the form stress D_p for the same wave modes as those shown in figure 18.

based on field measurements. By using this relation, we obtain a convection speed U_c of about 162 cm s^{-1} (where $u_a^* \sim 9$ cm s^{-1}) which is close to the mean wind speed in the simulated logarithmic layer where $U_a \sim 170 \pm 20$ cm s^{-1}. Figure 20(*a*) compares the mean square water-surface elevation from our simulation $\langle \eta^2 \rangle$ and the prediction $\langle \xi^2 \rangle$ from (7.1). Our simulated growth rate is larger than the theoretical prediction by a factor of about 1.5. The other three simulations shown in figure 20(*b–d*) will be described in § 8.

7.2. *Exponential growth stage*

Many theories have been proposed to explain the exponential growth of wind-generated surface waves. By examining the various processes that generate the asymmetric pressure perturbation at the surface, Belcher & Hunt (1993) show that the term induced by the thickening of the perturbed boundary layer on the leeside of the wave crests, which is called the non-separated sheltering effect, dominates. Furthermore, they relate the asymmetric effects to the drag force on the wave. When the asymmetric effect grows with time, it also increases the form stress on waves. This way, the form stress can play an important role in the exponential wave growth stage.

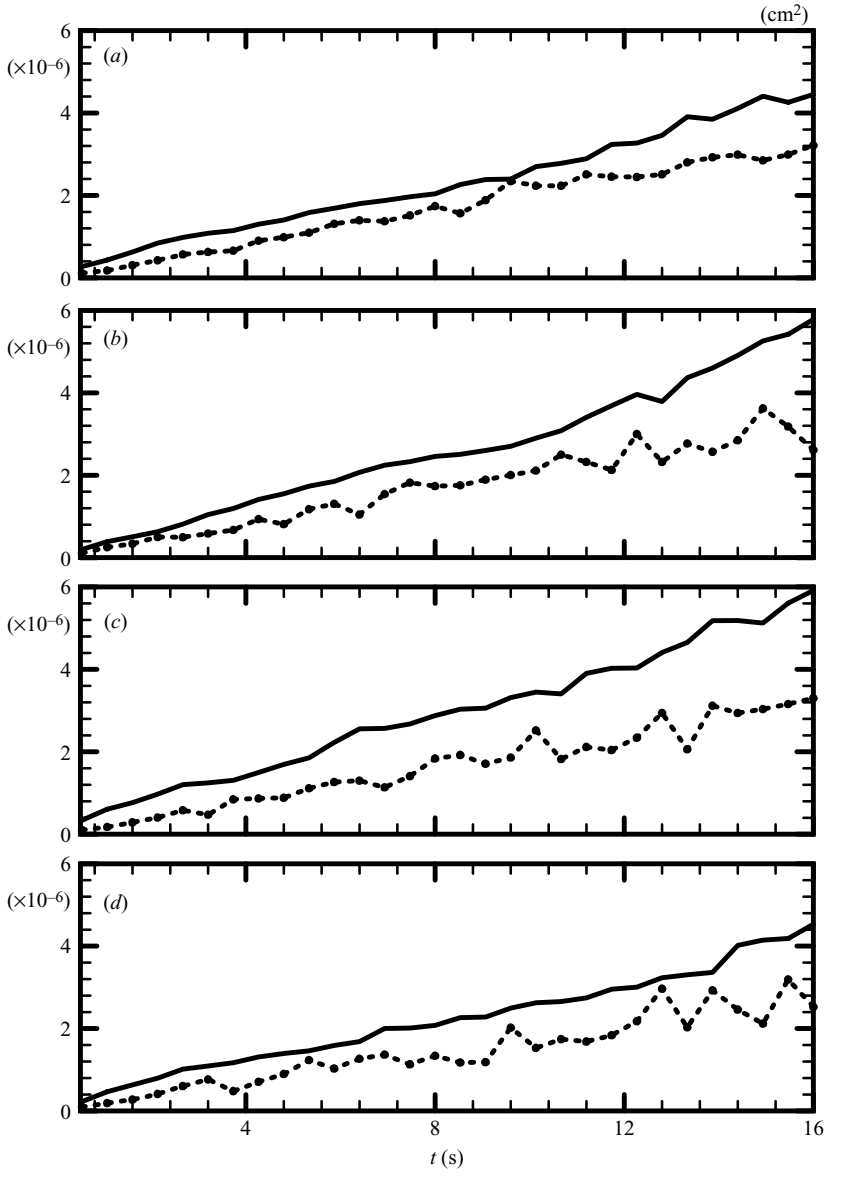

FIGURE 20. Comparison of the mean square water-surface elevations between our simulations $\langle \eta^2 \rangle$ (solid lines) and the theoretical predictions $\langle \xi^2 \rangle$ (dashed-dotted lines) of Phillips (1957). (*a*) The control run with the height of the air domain $h = 4\,\mathrm{cm}$, (*b*) the run with no initial turbulence in the water, (*c*) the run with no surface tension, and (*d*) the run with the height of the air domain $h = 8\,\mathrm{cm}$. For the theoretical curves, $U_c = 18u_a^*$ is used.

Here, we calculate the growth rate of our simulated waves and compare it to measurements synthesized by Plant (1982) and to theoretical (Belcher & Hunt 1993; Li 1995) and numerical studies that used a prescribed wavy surface (Sullivan & McWilliams 2002). The wave growth rate is defined as

$$\beta^* = \frac{2}{a}\frac{\mathrm{d}a}{\mathrm{d}t} = \frac{1}{E}\frac{\mathrm{d}E}{\mathrm{d}t}, \tag{7.3}$$

where β^* is dimensional wave growth rate, a is wave amplitude and $E = 0.5\rho_w a^2 c^2 k$ is wave energy density. Since the form stress dominates the contribution of energy input from the perturbed air flow to surface waves, the dimensionless wave growth rate β (where $\beta = \beta^*/\sigma$ and σ is wave frequency) computed from the right-hand side of (7.3) can also be expressed as (Li 1995)

$$\beta = \frac{1}{\sigma E}\frac{\mathrm{d}E}{\mathrm{d}t} = \frac{2}{\rho_w}\frac{D_p}{(ak)^2}\left(\frac{1}{c}\right)^2, \tag{7.4}$$

where the relation between the rate of change of the wave energy, $\mathrm{d}E/\mathrm{d}t$, and the form stress, D_p, is given as $\mathrm{d}E/\mathrm{d}t = cD_p$. We compute the growth rates from (7.3) and (7.4) and examine the contribution of form stress to wave growth. The one computed directly from wave amplitude is used to verify the contribution of form stress on wave growth. Figure 21(*a*) shows the time averaging ($t = 56$–70 s) of the growth rates of the three fast-growing wave components from our simulation. The growth rates calculated directly from the wave amplitude equation (7.3) (shown by the cross symbols) and those computed from the form stress equation (7.4) (shown by large triangle symbols) are similar to each other. For some wave modes the rates are close to the measurements synthesized by Plant (1982) and the simulation results that used a prescribed wavy surface from Li (1995) and Sullivan & McWilliams (2002), but others are 2–3 times larger than the measurements and theoretical predictions. The other three simulations shown in figure 21(*b–d*) are described in § 8.

The consistency of the growth rates calculated from wave amplitude and form stress supports Belcher & Hunt's (1993) argument that the form stress dominates the contribution of energy input from air to waves at the exponential wave growth stage.

8. Sensitivity tests

To study other possible mechanisms that may influence the simulated wave growth processes, we perform three sensitivity tests to examine the effects of turbulence in the water, surface tension and different computational domain sizes.

The first sensitivity test was motivated by Teixeira & Belcher's (2006) study. Teixeira & Belcher developed an analytical model to test the influence of turbulence in the air and in the water, separately, on surface wave growth. They suggested that turbulence in the water may play an important role, more than that suggested by Phillips (1957). To test their finding, we set up a simulation that consists of no turbulence in the water at the beginning of the simulation (that is, at our initialization procedure described in § 2.5 we do not allow for turbulence in the water to spin up before the interface starts to deform). Figure 20(*b*) compares its linear growth rate with the theoretical prediction by Phillips (1957) and figure 21(*b*) compares its exponential growth rate with measurements synthesized by Plant (1982). The linear growth rate is similar to, but slightly larger than, that of the control run with turbulence in the water to begin with (when we compare figures 20*a* and 20*b*). Figures 21(*a*) and 21(*b*) indicate that with or without turbulence in the water there is no significant difference in the exponential growth stage. Similarly to the control case, this case also shows a wide spread of wave energy in the wavenumber space at the early stage ($t = 16$ s, figure 22*c*), but then at the exponential growth stage ($t = 66$ s, figure 22*d*) energy begins to concentrate on just a few dominant wave components and these dominant waves have similar wavelengths as those found in the control case.

In the second sensitivity test, the surface tension in the interfacial boundary condition equation (2.9) is set to zero. The computed linear growth rate (figure 20*c*) is

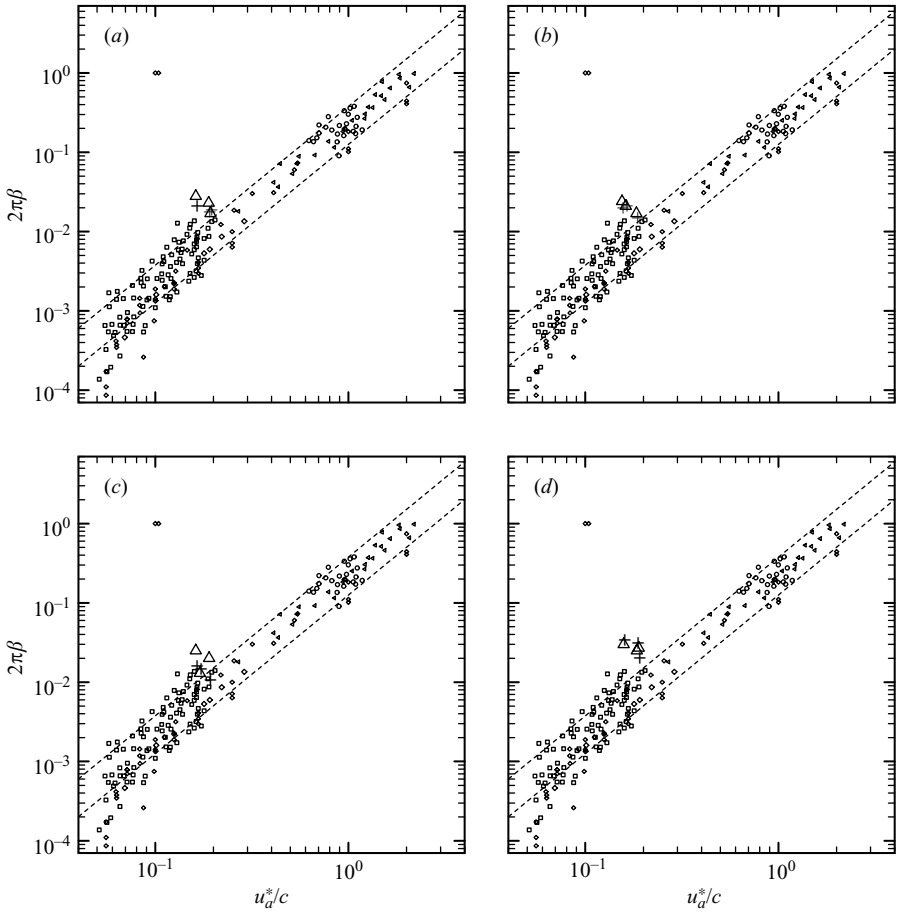

FIGURE 21. Wave growth rates as a function of inverse wave age. Small symbols are results from the measurements synthesized by Plant (1982) and simulation results that used a prescribed wavy surface (Li 1995; Sullivan & McWilliams 2002) as published in Sullivan & McWilliams (2002). The dashed lines are the empirical formula $\beta = (0.04 \pm 0.02)(u_*/c)^2$ proposed by Plant (1982). The cross and large triangle symbols are our results calculated directly from the growth of wave amplitude (7.3) and from the form stress (7.4), respectively, for the three fast-growing wave components. The three fast-growing wave components are $(k_x, k_y) = (0.78, 0)$, $(0.52, 0)$ and $(0.78, 0.26)\,\mathrm{cm}^{-1}$ for the control simulation (*a*); $(0.52, 0)$, $(0.78, 0.26)$ and $(0.52, 0.26)\,\mathrm{cm}^{-1}$ for the simulation with no initial turbulence in the water (*b*); $(0.78, 0)$, $(0.52, 0.26)$ and $(0.52, 0)\,\mathrm{cm}^{-1}$ for the simulation with no surface tension (*c*); and $(0.52, 0)$, $(0.78, 0)$ and $(0.78, 0.26)\,\mathrm{cm}^{-1}$ for the simulation with larger air domain (*d*).

slightly higher than that of the control case with surface tension, but its exponential growth rate (figure 21*c*) is similar to the previous runs. The distributions of wave energy spectra (figure 22*e*, *f*) also exhibit similar patterns to those from the simulation with surface tension (figure 22*a*, *d*). Kundu (1990) suggests that waves with wavelengths smaller than 0.4 cm are affected by the surface tension and waves larger than 7 cm are dominated by gravity. According to Kundu (1990), we can categorize waves into capillary waves ($\lambda < 0.4\,\mathrm{cm}$), gravity–capillary waves ($\lambda = 0.4 \sim 7\,\mathrm{cm}$) and gravity waves ($\lambda > 7\,\mathrm{cm}$). The waves we generated here have wavelengths ranging between 8 and 10 cm, which belong to gravity waves. Furthermore, during this initial growth stage (before the interface of the coupled model becomes too nonlinear), we

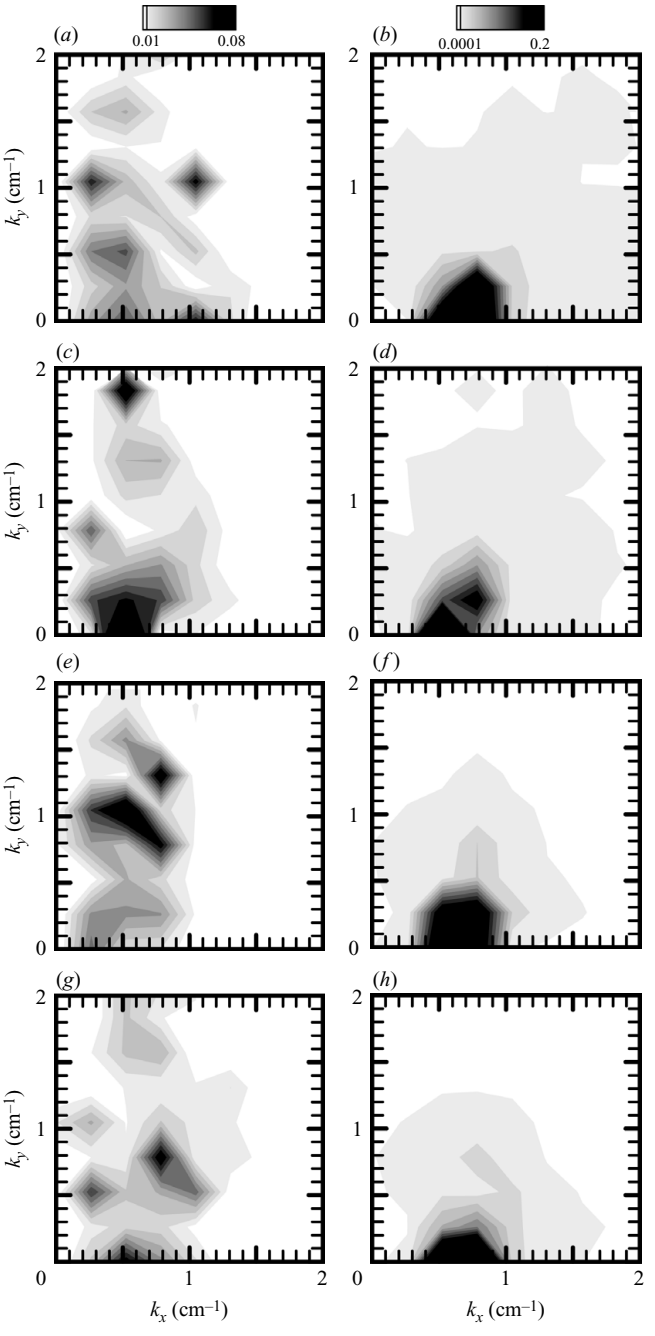

FIGURE 22. Spectra of water surface elevation $\hat{\eta}(k_x, k_y)$ (normalized by its total energy) at time $t = 16$ s (a, c, e, g) and $t = 66$ s (b, d, f, h) for (a, b) the control case; (c, d) the simulation without turbulence in the water at the beginning of the simulation; (e, f) the simulation without surface tension at the interface; and (g, h) the simulation doubling the height of the computational domain of the air.

did not observe any small capillary waves embedded on the long gravity waves in the simulations with surface tension. Thus, whether there is surface tension or not makes no significant difference to the wave growth we study here.

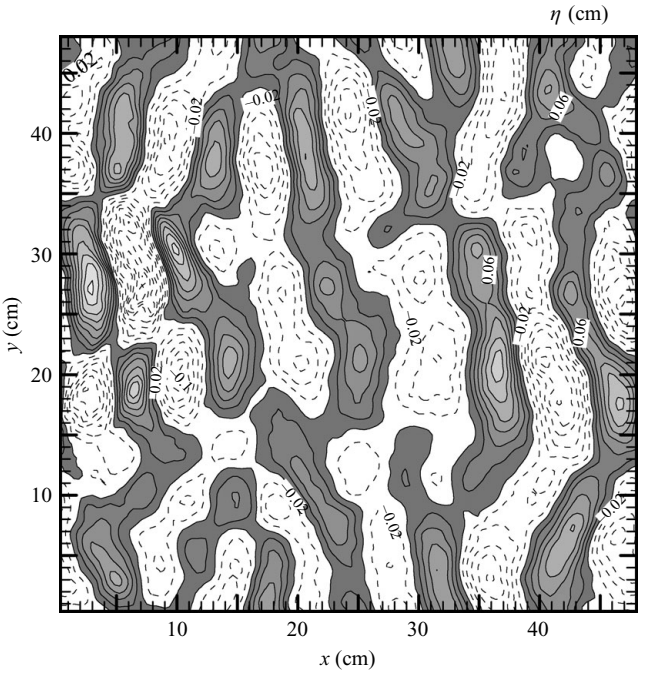

FIGURE 23. Snapshot of the water surface elevation at $t = 64$ s. This simulation is the same as the control run except that it uses a larger horizontal domain of $L_x = L_y = 48$ cm. The wavelength in the streamwise direction is similar to that found in figure 5(*c*). The time period of this simulation run is nearly 65 s.

For the third sensitivity test, we perform several simulations with different domain sizes to see whether the dominated waves stay the same. First, we double the domain height of the air to $h_a = 8$ cm while keeping vertical resolution and horizontal domain the same. The linear wave growth rate is similar to that of the control run (figures 20*a* *vs.* 20*d*) and comparable to the theoretical predication of Phillips (1957). However, the wave growth rates at the exponential growth stage, shown as the cross and large triangle symbols in figure 21(*d*), are slightly larger than the other simulations and also larger than theoretical predictions. Nevertheless, the wave energy spectra (figure 22*g*, *h*) look similar to those of the previous three cases. We also change the size of the horizontal domain to $L_x = L_y = 48$ cm while keeping the same horizontal resolution as the control run. Figure 23 shows a snapshot of the water-surface elevations at $t = 64$ s; the wavelength of dominant waves is also about 8–12 cm, which is similar to the control run. Some other runs with domain sizes of $L_x = L_y = 12$, 16, 20 and 36 cm also reveal similar results (not shown here). Hence, we conclude that the horizontal domain of the model does not influence the wavelength of the dominated waves excited by the wind in our simulations, and the choice of the domain size for simulations is not an important factor to influence wind-wave generation processes.

9. Conclusions

The initial wind-wave generation processes consist of linear and exponential growth stages as proposed by theoretical studies and supported by some laboratory and field measurements, but these processes have never been studied by numerical simulation before. In this study, we developed an air–water coupled model where the continuity

of velocity and stress is satisfied at the interface, so it can simulate the interaction of two fully developed turbulent layers (air and water) above and below the interface. The limitation of our coupled model is the linearization of the interfacial boundary conditions and hence the model is applicable only to small-amplitude waves.

The characteristics of simulated waves are similar to field and laboratory observation at the initial stage of wind-wave generation. The wavelength of the dominated waves is about 8 cm which is in the range of wind-induced gravity waves. The corresponding wave age $c/u_a^* \sim 5$ belongs to 'young sea' or 'slow moving waves'.

At the early stage of wave growth, the turbulent flow structures in the air (and in the water) remain similar to shear-driven turbulent flows over a flat surface (and under a flat free surface). At the later stage of our simulation, waves grow exponentially and the flow fields are strongly influenced by wave motions. The effects of flow fields by waves are summarized as follows. (i) The streaky structure, which is a typical phenomenon of shear-driven turbulent flow, is interrupted by wave motions and the streamwise velocity field forms a pocket-like feature. (ii) The flow field over the whole water domain is strongly affected by the waves at the later stage. This effect is evidenced from the iso-surface of vertical velocity, the vertical profiles of the mean velocity and turbulence intensity. (iii) Wave effects to the velocity field in the air are confined only in the thin viscous sublayer. The turbulence intensity of the air does not change significantly owing to waves. (iv) The pressure field in the air behaves differently at the early and later stages. At the early stage, the pressure fluctuations of the air are mainly turbulence-induced and advect faster than the phase velocity of waves. At the later stage, the air pressure fluctuations become waveform throughout the turbulent layer and move along with the surface waves.

Similar to the theoretical studies, our simulated waves can be separated into linear and exponential growth stages as distinguished by the following flow behaviours: (i) the behaviour of pressure fluctuations of the air (which are considered to be the main factor that is available to initiate and support wave motion); (ii) the simulated interfacial properties; (iii) the growth trend, and (iv) the magnitude of the form stress (which is considered to be the main contributor of energy transfer from wind to waves at the exponential growth stage).

We compared our growth rates to theoretical predictions, field and laboratory measurements, or other numerical simulations that used a prescribed wavy surface. At the linear growth stage, the theoretical prediction from Phillips' (1957) wind-wave generation mechanism is examined. Our wave growth rates are about 1–2 times larger than the theoretical prediction. At the exponential growth stage, our wave growth is consistent with Belcher & Hunt's (1993) non-separated sheltering mechanism because our $c/u_* < 5$. However, the growth rates computed from our simulated waves are somewhat larger (by a factor of about 2) than those obtained from measurements (Plant 1982), simulations that used a prescribed wavy surface (Sullivan & McWilliams 2002; Li 1995) and Belcher & Hunt's (1993) theoretical prediction.

This work was mainly supported by grants from the National Science Council of Taiwan under contract numbers NSC 90-2611-M-009-001 and 91-2611-M-008-002. The National Center for Atmospheric Research is sponsored by the National Science Foundation.

REFERENCES

Al-Zanaidi, M. A. & Hui, W. H. 1984 Turbulent airflow over water waves – a numerical study. *J. Fluid Mech.* **148**, 225–246.

Aydin, E. M. & Leutheusser, H. J. 1991 Plane-Couette flow between smooth and rough walls. *Exps. Fluids* **11**, 302–312.

Belcher, S. E. & Hunt, J. C. R. 1993 Turbulent shear flow over slowly moving waves. *J. Fluid Mech.* **251**, 109–148.

Belcher, S. E., Newley, T. M. J. & Hunt, J. C. R. 1993 The drag on an undulating surface due to the flow of a turbulent layer. *J. Fluid Mech.* **249**, 557–596.

Caulliez, G. & Collard, F. 1999 Three-dimensional evolution of wind waves from gravity–capillary to short gravity range. *Eur. J. Mech.* B/*Fluids* **13**, 389–402.

Chandrasekhar, S. 1954 The character of the equilibrium of an incompressible heavy viscous fluid of variable density. *Q. J. Mech.* 162–178.

Cheung, T. K. & Street, R. L. 1988 The turbulent layer in the water at an air–water interface. *J. Fluid Mech.* **194**, 133–151.

Choy, B. & Reible, D. D. 2000 *Diffusion Model of Environmental Transport*. Lewis.

Davis, R. E. 1970 On the turbulent flow over a wavy boundary. *J. Fluid Mech.* **42**, 721–731.

De Angelis, V., Lombardi, P. & Banerjee, S. 1997 Direct numerical simulation of turbulent flow over a wavy wall. *Phys. Fluids* **9**, 2429–2442.

De Angelis, V. 1998 Numerical investigation and modeling of mass transfer processes at sheared gas–liquid interface. PhD thesis, UCSB.

van Duin, C. A. & Jassen, P. A. E. M. 1992 An analytic model of the generation of surface gravity waves by turbulent air flow. *J. Fluid Mech.* **236**, 197–215.

Fulgosi, M., Lakehal, D., Banerjee, S. & De Angelis, V. 2003 Direct numerical simulation of turbulence in a sheared air–water flow with a deformable interface. *J. Fluid Mech.* **482**, 319–345.

Gent, P. R. & Taylor, P. A. 1976 A numerical model of the air flow above water waves. *J. Fluid Mech.* **77**, 105–128.

Henn, D. S. & Sykes, R. I. 1999 Large-eddy simulation of flow over wavy surface. *J. Fluid Mech.* **383**, 75–112.

Howe, B. M., Chambers, A. J., Klotz, S. P., Cheung, T. K. & Street, R. L. 1982 Comparison of profiles and fluxes of heat and momentum above and below an air–water interface. *Trans. ASME* C: *J. Heat Transfer* **104**, 34–39.

Jacobs, S. J. 1987 An asymptotic theory for the turbulent flow over a progressive wave. *J. Fluid Mech.* **174**, 69–80.

Jeffreys, H. 1925 On the formation of water waves by wind. *Proc. R. Soc. Lond.* A **107**, 189–206.

Kahma, K. K. & Donelan, M. A. 1988 A laboratory study of the minimum wind speed for wind wave generation. *J. Fluid Mech.* **192**, 339–364.

Kawai, S. 1979 Generation of initial wavelets by instability of a coupled shear flow and their evolution to wind waves. *J. Fluid Mech.* **93**, 661–703.

Kim, J., Moin, P. & Moser, R. 1987 Turbulence statistics in fully developed channel flow at low Reynolds number. *J. Fluid Mech.* **177**, 133–166.

Kundu, P. K. 1990 *Fluid Mechanics*. Academic.

Larson, T. R. & Wright, J. W. 1975 Wind-generated gravity–capillary waves: laboratory measurements of temporal growth rates using microwave backscatter. *J. Fluid Mech.* **70**, 417–436.

Li, P. Y. 1995 A numerical study on energy transfer between turbulent air flow and finite amplitude water waves. PhD thesis, York University.

Lombardi, P., De Angelis, V. & Banerjee, S. 1996 Direct numerical simulation of near-interface turbulence in coupled gas–liquid flow. *Phys. Fluids* **8**, 1643–1665.

Massel, S. R. 1996 *Ocean Surface Waves: their Physics and Prediction*. World Scientific.

Miles, J. W. 1957 On the generation of surface waves by shear flows. *J. Fluid Mech.* **3**, 185–204.

Moin, P. & Mahesh, K. 1998 Direct numerical simulation: a tool in turbulence research. *Annu. Rev. Fluid Mech.* **30**, 539–578.

Papavassiliou, D. V. & Hanratty, T. J. 1997 Interpretation of large-scale structures observed in a turbulent plane Couette flow. *Intl J. Heat Fluid Flow* **18**, 55–69.

Phillips, O. M. 1957 On the generation of waves by a turbulent wind. *J. Fluid Mech.* **2**, 417–445.

Phillips, O. M. 1977 *Dynamics of the Upper Ocean*. Cambridge University Press.

Phillips, O. M. & Katz, E. J. 1961 The low frequency components of the spectrum of wind generated waves. *J. Mar. Res.* **19**, 57–69.

Plant, W. J. 1982 A relationship between wind stress and wave slope. *J. Geophys. Res.* **87**, 1961–1967.

Plate, E. J., Chang, P. C. & Hidy, G. M. 1969 Experiments on the generation of small water waves by wind. *J. Fluid Mech.* **35**, 625–656.

Spalart, P. R., Moser, R. D. & Rogers, M. M. 1991 Spectral methods for the Navier–Stokes equations with one infinite and two periodic directions. *J. Comput. Phys.* **96**, 297–324.

Sullivan, P. P. & Mcwilliams, J. C. 2002 Turbulent flow over water waves in the presence of stratification. *Phys. Fluids* **14**, 1182–1195.

Sullivan, P. P., Mcwilliams, J. C. & Moeng, C. H. 2000 Simulation of turbulent flow over idealized water waves. *J. Fluid Mech.* **404**, 47–85.

Sullivan, P. P., Mcwilliams, J. C. & Melville, W. K. 2004 The oceanic boundary layer driven by wave breaking with stochastic variability. Part 1. Direct numerical simulations. *J. Fluid Mech.* **507**, 143–174.

Teixeira, M. A. C. & Belcher, S. E. 2006 On the initiation of surface waves by turbulent shear flow. *Dyn. Atmos. Oceans* **41**, 1–27.

Townsend, A. A. 1972 Flow in a deep turbulent boundary layer over a surface distorted by water waves. *J. Fluid Mech.* **55**, 719–735.

Townsend, A. A. 1980 Sheared turbulence and additional distortion. *J. Fluid Mech.* **98**, 171–191.

Tsai, W.-T. 1998 A numerical study of the evolution and structure of a turbulent shear layer under a free surface. *J. Fluid Mech.* **354**, 239–276.

Tsai, W.-T. & Yue, D. K. P. 1995 Effect of soluble and insoluble surfactant on laminar interactions of vortical flows with a free surface. *J. Fluid Mech.* **289**, 315–349.

Tsai, W.-T., Chen, S.-M. & Moeng, C.-H. 2005 A numerical study on the evolution and structure of a stress-driven free-surface turbulent shear flow. *J. Fluid Mech.* **545**, 163–192.

Veron, F. & Melville, W. K. 2001 Experiments on the stability and transition of wind-driven water surfaces. *J. Fluid Mech.* **446**, 25–65.

Wehausen, J. V. & Laitone, E. V. 1960 Surface waves. In *Handbook of Physics*, vol. 9, pp. 446–778. Springer.